PABPC1L Induces IDO1 to Promote Tryptophan Metabolism and Immune Suppression in Renal Cell Carcinoma

Guannan Shu[1,2], Minyu Chen[1], Wuyuan Liao[1], Liangmin Fu[1], Mingjie Lin[1], Chengpeng Gui[1], Junjie Cen[1], Jun Lu[1], Zhenhua Chen[1], Jinhuan Wei[1], Wei Chen[1], Yinghan Wang[1], Jiangquan Zhu[1], Tianxin Zhao[2,3], Xiaonan Liu[4], Jiajia Jing[5], Guo-chang Liu[2], Yihui Pan[6], Junhang Luo[1], and Jiaxing Zhang[7]

ABSTRACT

The tumor microenvironment (TME) in renal cell carcinomas (RCC) is marked by substantial immunosuppression and immune resistance despite having extensive T-cell infiltration. Elucidation of the mechanisms underlying immune evasion could help identify therapeutic strategies to boost the efficacy of immune checkpoint blockade (ICB) in RCC. This study uncovered a mechanism wherein the polyadenylate-binding protein PABPC1L modulates indoleamine 2,3-dioxygenase 1 (IDO1), a prospective target for immunotherapy. *PABPC1L* was markedly upregulated in RCC, and high *PABPC1L* expression correlated with unfavorable prognosis and resistance to ICB. PABPC1L bolstered tryptophan metabolism by upregulating IDO1, inducing T-cell dysfunction and Treg infiltration. PABPC1L enhanced the stability of *JAK2* mRNA, leading to increased JAK2-STAT1 signaling that induced IDO1 expression. Additionally, PABPC1L-induced activation of the JAK2-STAT1 axis created a positive feedback loop to promote *PABPC1L* transcription. Conversely, loss of *PABPC1L* diminished *IDO1* expression, mitigated cytotoxic T-cell suppression, and enhanced responsiveness to anti-PD-1 therapy in patient-derived xenograft models. These findings reveal the crucial role of PABPC1L in facilitating immune evasion in RCC and indicate that inhibiting PABPC1L could be a potential immunotherapeutic approach in combination with ICB to improve patient outcomes.

Significance: PABPC1L functions as a key factor in renal cell carcinoma immune evasion, enhancing IDO1 and impeding T-cell function, and represents a potential target to enhance the efficacy of immune checkpoint blockade therapy.

Introduction

Renal cell carcinoma (RCC), a prevalent malignant tumor in the urinary system, is increasingly common, constituting about 4.1% of all new cancer cases in the United States in 2022 (1). While early-stage RCC is typically treated with surgery, about 30% of patients experience recurrence or metastasis. For metastatic RCC, immune checkpoint blockade (ICB) therapy has been effective for some, but around 75% of patients show resistance, and even responsive patients eventually face progression (2). Current first-line treatments combine ICB with tyrosine kinase inhibitors, yet most patients develop drug resistance (3, 4). Therefore, identifying drivers of immune evasion and new therapeutic targets to enhance ICB responsiveness in RCC is crucial.

RCC has long been recognized as a "hot" cancer, frequently exhibiting a high degree of immune infiltration (5, 6). A comprehensive study employing mass cytometry for in-depth immune profiling of the primary RCC tumor microenvironment (TME) revealed extensive infiltration of PD-1+ T cells in RCC and there is an association between the expression of T-cell exhaustion markers and survival outcomes (7). Moreover, a proteogenomic analysis of RCC from 232 Chinese patients demonstrated that the GP1 subtype, characterized by the most pronounced immunosuppressive features, is linked to the poorest clinical outcomes (8). These findings suggest that immune evasion is prevalent among patients with RCC and plays a crucial role in determining long-term survival.

The essential amino acid tryptophan (TRP) depletion and the subsequent increase in kynurenine (KYN) levels detrimentally affect effector T-cell functionality, substantially aiding in the development of peripheral immune tolerance (9). Indoleamine 2,3-dioxygenase 1 (IDO1), a key enzyme, orchestrates the breakdown of TRP to KYN, playing a pivotal role in immune regulation (10). IDO1-mediated TRP metabolism within the KYN pathway is among the most widely studied metabolic pathways associated with immune tolerance and tumor cell immune evasion (11, 12). Elevated expression of *IDO1* fosters an immunosuppressive TME by deactivating T cells and natural killer (NK) cells, while simultaneously encouraging the growth and function

[1]Department of Urology, The First Affiliated Hospital of Sun Yat-sen University, Guangzhou, P.R. China. [2]Department of Urology, Guangzhou Women and Children's Medical Center, Guangzhou Medical University, Guangdong Provincial Clinical Research Center for Child Health, Guangzhou, P.R. China. [3]Department of Pediatric Surgery, Guangzhou Institute of Pediatrics, Guangdong Provincial Key Laboratory of Research in Structural Birth Defect Disease, Guangzhou Women and Children's Medical Center, Guangzhou Medical University, Guangzhou, Guangdong, P.R. China. [4]Center for Reproductive Medicine, Guangzhou Women and Children's Medical Center, Guangzhou Medical University, Guangzhou, P.R. China. [5]The First Affiliated Hospital, Sun Yat-sen University, Guangzhou, P.R. China. [6]Department of Urology, the Third Affiliated Hospital, Soochow University, Changzhou, Jiangsu, P.R. China. [7]Department of Oncology, The First Affiliated Hospital, Sun Yat-sen University, Guangzhou, P.R. China.

G. Shu, M. Chen, W. Liao, L. Fu, and M. Lin contributed equally to this article.

Corresponding Authors: Jiaxing Zhang, First Affiliated Hospital of Sun Yat-sen University, No.58, Zhongshan Second Road, Guangzhou, Guangdong 510000, P. R. China. E-mail: zhangjx25@mail.sysu.edu.cn; Guochang Liu, starbless2003@126.com; Yihui Pan, panyihui0314@163.com; and Junhang Luo, luojunh@mail.sysu.edu.cn

Cancer Res 2024;84:1659–79

doi: 10.1158/0008-5472.CAN-23-2521

of regulatory T cells (Treg) and myeloid-derived suppressor cells (MDSC; refs. 9, 13, 14). In addition, the interaction of KYN and its derivatives with the aryl hydrocarbon receptor (AhR) activates AhR signaling pathways, leading to a multitude of immune-modulatory outcomes. These include an increase in *IDO1* expression within tumor cells, heightened programmed cell death 1 (*PD-1*) levels on $CD8^+$ T cells, enhanced forkhead box P3 (*FOXP3*) expression in $CD4^+$ T cells, restricted $CD8^+$ T-cell proliferation, and an expanded Treg fraction, thereby significantly altering the immune response within the TME (15–19).

Poly(A) binding protein cytoplasmic 1 like (*PABPC1L*), a member of the polyadenylate-binding protein family, modulates mRNA stability and translation. The murine ortholog of this gene is required for female fertility (20). In recent years, accumulating evidence has demonstrated that *PABPC1L* plays a crucial regulatory role in cancers. In colorectal cancer, *PABPC1L* is a significant prognostic marker, promoting invasion, and metastasis via the AKT pathway (21). It also holds prognostic value in prostate cancer (22). Our latest findings reveal that *PABPC1L* represents one of the molecular hallmarks of hypoxia-induced immunosuppression in RCC (23). Herein, our findings demonstrate that PABPC1L interacts with *JAK2* mRNA and enhances its translation. The interaction between PABPC1L and *JAK2* mRNA protects *JAK2* mRNA from rapid degradation by nucleases and facilitates the binding of *JAK2* mRNA to the eukaryotic translation initiation complex, thereby promoting the efficient translation of *JAK2* mRNA into protein. Furthermore, the combined inhibition of *PABPC1L* and ICB therapy results in a significantly enhanced antitumor effect in RCC preclinical patient-derived xenograft (PDX) models compared with monotherapy. Collectively, our study reveals the critical role of *PABPC1L* in promoting immune evasion by upregulating JAK2/STAT1/IDO1 signaling, potentially serving as a complementary approach to ICB therapy in RCC.

Materials and Methods

Patients and specimens

All human RCC tissue specimens were obtained from the Department of Urology, the First Affiliated Hospital, Sun Yat-sen University (SYSU; Guangzhou, P.R. China). The protocol was approved by the Medical Ethics Committee of the First Affiliated Hospital, Sun Yat-sen University [approval number LS(2021)143]. Patients provided written informed consent, and the study was carried out according to the Declaration of Helsinki. RCC tissues treated with RNAlater and stored at −20°C were used for qRT-PCR analyses. RCC tissues stored at −80°C were used for Western blotting analyses.

Cell culture

The immortalized renal epithelial cell line (HK-2, RRID: CVCL_YE28), the human RCC cell lines [786-O (RRID: CVCL_1051), 769-P (RRID: CVCL_1050), A-498 (RRID:CVCL_1056), ACHN (RRID: CVCL_1067), and Caki-1 (RRID:CVCL_0234)] and the mouse RCC cell line (Renca, RRID:CVCL_2174) were purchased from ATCC. The human embryonic kidney 293T cell line (RRID: CVCL_0063) was purchased from the Cell Bank of the Chinese Academy of Sciences. The HK-2 cell line was cultured in Keratinocyte Serum-free Medium (SFM). The 293T and ACHN cell lines were cultured in DMEM. The Caki-1 cell line was cultured in McCoy's 5A Medium. The remaining RCC cell lines were cultured in RPMI1640 medium. All media were obtained from Gibco and supplemented with 1% penicillin–streptomycin (Biosharp Biotechnology) and 10% FBS (BioChannel). All cell lines were examined with short tandem repeat profiling by the vendors and routinely tested for *Mycoplasma* infection.

Isolation of primary RCC cells

Tumor tissues, which were pathologically diagnosed as RCC, were isolated and washed with cold PBS (supplemented with 2% penicillin–streptomycin solution). The tumors were then cut into pieces and digested in DMEM containing 0.002% DNase I (Stemcell), 0.01% hyaluronidase (Stemcell), 0.2% collagenase IV (Stemcell), and 3×10^{-3} mol/L $CaCl_2$ (21115, Sigma-Aldrich) at 37°C for 60 minutes with continuous shaking at 200 rpm. The digestion was centrifuged at $300 \times g$, and the supernatant was filtered through a 40 μm cell strainer (352340, Corning). The cell suspension was cultured in a 6-well plate with DMEM containing 10% FBS and 1% penicillin–streptomycin solution.

Isolation of tumor-infiltrating cells and lymphoid cells

Isolation of tumor-infiltrating lymphoid cells has been described previously (24). Tumor samples were minced with scissors before incubation with 1.67 U mL^{-1} Liberase (Roche) and 0.2 mg mL^{-1} DNase (Roche) in RPMI for 30 minutes at 37°C. Samples were then processed by repeated pipetting and filtered through a 100-μm nylon filter (BD Biosciences) in RPMI to generate single-cell suspensions, which were subsequently washed with complete RPMI and purified on a Ficoll gradient to enrich T cells. Single-cell suspensions from spleens were obtained by grinding spleens through 40-μm filters. When required, samples were treated with red blood cell lysis buffer (ACK Lysing Buffer, Lonza) and further washed and resuspended in FACS buffer (PBS/0.5%albumin) before incubation with antibodies. For the isolation of intratumoral $CD8^+$ T cells, shCtrl and shPABPC1L tumors were excised and dissected into single-cell suspensions. Tumor-isolated $CD8^+$ T cells were enriched by Ficoll gradient (Sigma-Aldrich) before sorting as ($CD45^+CD3^+CD8^+$) on a FACSAriaTM II Cell Sorter (BD Biosciences).

Three-dimensional killing assay

Tumor-infiltrating $CD8^+$ T cells were generated as described above and the three-dimensional (3D) collagen-fibrin gel–based killing assay has been previously described in depth (25). In brief, 0.1×10^5 viable target cells were co-embedded into collagen-fibrin gels with 1×10^5 FACS-sorted infiltrating $CD8^+$ T cells in a 10: 1 ratio (effector: target). αCD3/CD28-activated $CD8^+$ splenic T cells were used as a positive control. After 48 hours of coculture, collagen-fibrin gels were dissolved and target cells were diluted and plated for a colony formation assay. After 7 days, cells were fixed using 3.7% formaldehyde and stained with 2% methylene blue before colony counting.

Methods for measuring granzyme B

Isolation of tumor-infiltrating lymphoid cells was described above and cells were stimulated with 50 ng/mL phorbol 12-myristate 13-acetate (PMA), 1 μmol/L ionomycin, and 5 μg/mL Brefeldin A for 4 hours at 37°C and were then treated with fixation buffer and permeabilization buffer and stained for intracellular granzyme B (GZMB) with anti-human/mouse GZMB for 20 minutes at 4°C in the dark. Cells were washed and suspended in 200 μL FACS buffer for flow cytometry analysis.

Antibodies and reagents

The following primary antibodies were utilized in the Western blot and immunoprecipitation analyses: JAK1 (3344, Cell Signaling Technology, CST, RRID:AB_2265054), p-JAK1 (74129, CST, RRID:

AB_2799851), JAK2 (3230, CST, RRID:AB_2128522), p-JAK2 (3771, CST, RRID:AB_330403), STAT1 (14994, CST, RRID:AB_2737027), pSTAT1 (9167, CST, RRID:AB_561284), STAT3 (9139, CST, RRID:AB_331757), pSTAT3 (9145, CST, RRID:AB_2491009), anti-human PABPC1L (Abcam, ab233280), EIF4G (2469, CST, RRID:AB_2096028), Flag tag (AE005, ABclonal, RRID:AB_2770401), His tag (AE003, ABclonal, RRID:AB_2728734), mouse control IgG (AC011, ABclonal, RRID:AB_2770414), rabbit control IgG (AC005, ABclonal, RRID:AB_2771930), IDO1 (A12125, ABclonal), and GAPDH(60004-1-Ig, Proteintech, RRID:AB_2107436). The following antibodies were used for IHC staining: anti-human PABPC1L (Abcam, ab233280) and cleaved caspase-3 (9661, CST, RRID:AB_2341188). The secondary antibodies used in the immunofluorescence (IF) assay were as follows: CoraLite488 (SA00013-2, Proteintech, RRID:AB_2797132) and CoraLite594 (SA00013-3, Proteintech, RRID:AB_2797133). The following antibodies were used for flow cytometry analyses: FITC anti-human CD8a (300905, BioLegend, RRID:AB_314110), PE anti-mouse CD8a (162303, BioLegend, RRID:AB_2894434), FITC anti-mouse CD8a (100705, BioLegend, RRID:AB_312745), PE anti-mouse Perforin (154305, BioLegend, RRID:AB_2721639), PerCP/Cyanine5.5anti-human Perforin (308113, BioLegend, RRID:AB_2169092), FITC anti-human/mouse GZMB (372205, BioLegend, RRID:AB_2687029), PE antihuman/mouse GZMB (372207, BioLegend, RRID:AB_2687031), PE anti-mouse CD45 (147711, BioLegend, RRID:AB_2563597), FITC anti-mouse CD4 (100405, BioLegend, RRID:AB_312691), Alexa Fluor700 anti-mouse FOXP3 (126421, BioLegend, RRID:AB_2750492), APC anti-mouse CD19 (152409, BioLegend, RRID:AB_2629839), APC anti-mouse F4/80 (123115, BioLegend, RRID:AB_893493), FITC anti-mouse/human CD11b (101205, BioLegend, RRID:AB_312789), PE anti-mouse IFNγ (505807, BioLegend, RRID:AB_315401), PE anti-human IFNγ (502508, BioLegend, RRID:AB_315235), APC antihuman CD3 (317317, BioLegend, RRID:AB_1937213), APC anti-mouse CD3 (100235, BioLegend, RRID:AB_2561455), and FITC anti-human HLA-A2 (343303, BioLegend, RRID:AB_1659245).

Plasmid, RNAi, and lentivirus construction

Flag-tagged PABPC1L, Flag-tagged truncated PABPC1L, Flag-tagged full-length JAK2, and full-length STAT1 were cloned into the pcDNA3.1(+) vector (Genecopoeia). All the plasmids were sequenced before transfection to confirm the correct nucleotide sequence. siRNAs targeting PABPC1L, IDO1, and STAT1 for *in vitro* and *in vivo* experiments were synthesized by RiboBio. The short hairpin RNA (shRNA) lentivirus and overexpression lentivirus were constructed, identified, and provided by Bioyard Biotechnology. The targeted sequences are shown in Supplementary Table S1.

Primary human peripheral blood mononuclear cell and $CD8^+$ T-cell isolation

Peripheral blood mononuclear cells (PBMC) were isolated from healthy donors using FicollPaque (17-5442-02, GE Healthcare) density gradient centrifugation following the manufacturer's instructions, and PBMCs were washed twice with PBS. Primary human $CD8^+$ T cells were purified using a $CD8^+$ T-cell Isolation Kit (Miltenyi Biotec, 130-096-495) following the manufacturer's instructions. $CD8^+$ T cells were confirmed to be > 95%pure by flow cytometric analysis.

IDO1 knockout cell line construction

Construction of IDO1 knockout (KO) cell line has been described previously (12). To construct the IDO1 knockout cell line, we utilized CRISPR technology with guide RNAs for IDO1, designed using the CRISPR design platforms Deskgene and CRISPOR, ensuring a minimum of three mismatches at NGG PAM sites. The crRNA-tracrRNA duplex were prepared by mixing equimolar concentration of Alt-R crRNA, Alt-R tracrRNA, and ATTO550 (1075298, Integrated DNA Technologies) followed by heating at 95°C for 5 minutes and slowly cooled to room temperature. For assembly of the Cas9/RNP complex, this duplex was mixed with Alt-R S. p Cas9 nuclease V3 (1081059, Integrated DNA Technologies) and allowed to incubate at room temperature for 20 minutes. Cells were then prepared and mixed with the Cas9/RNP complex for a brief 2-minute incubation at room temperature before electroporation using a 4D-nucleofector system. Following a 48-hour posttransfection period, the cells underwent trypsinization and were suspended in PBS supplemented with 1% FBS for subsequent FACS. Cell clones became visible after 7 to 14 days of culture, at which point, genomic DNA was extracted for PCR analysis. The successful knockout of IDO1 was verified at both the mRNA and protein levels by comparing the IDO1-KO cells with the parental line through RT-PCR and Western blot analysis, respectively.

qRT-PCR analyses

Total RNA from tumor tissues or cell lines was extracted with TRIzol (Invitrogen). Total RNA was reverse transcribed using 4× Reverse Transcription Master Mix (EZBioscience) according to the manufacturer's instructions. qRT-PCR was performed using 2× SYBR Green qPCR Master Mix (EZBioscience) and a Roche LightCycler480 Instrument. The forward and reverse primers used in this study are listed in Supplementary Table S2.

Western blotting analysis

Cells were lysed in cell lysis buffer (Beyotime) with protease inhibitor cocktail (CoWin BioSciences) on ice and then collected with cell scrapers (BIOFIL). Protein quantitation was performed with Pierce bicinchoninic acid Protein Assay Kit (Thermo Fisher Scientific) and measured at a wavelength of 562 nm (MD VersaMax). Protein samples were loaded in 7.5%–12.5% SDS-PAGE gels. After electrophoresis, proteins were transferred to polyvinylidene difluoride (PVDF) membranes (Merck Millipore) in an electrophoretic transfer unit (Tanon). After blocking, the PVDF membranes were incubated with primary antibodies at 4°C for more than 12 hours. After 1 hour of incubation with secondary antibodies at room temperature, the protein bands were detected by chemiluminescence (Tanon).

Coimmunoprecipitation assay

Cells transfected with indicated plasmids were lysed in cell lysis buffer (Beyotime) with protease inhibitor cocktail (CoWin BioSciences). Ten percent of input were collected and stored at −20°C for the following analyses. Protein samples were incubated with protein A/G magnetic beads (Thermo Fisher Scientific) and antibodies at 4°C overnight. Wash the magnetic beads five times for 5 minutes and remove the supernant. Finally, 1 × SDS loading buffer was added to magnetic beads for protein denaturation. Immunoprecipitation (IP) samples were stored at −20°C or directly used for electrophoresis.

m^7GTP pulldown assay

For the pulldown assay, each tube was supplemented with 20 μL of m^7GTP agarose beads, which were subsequently washed thrice with IP buffer (50 mmol/L Tris-HCl, pH 7.5; 150 mmol/L NaCl; 1 mmol/L ethylenediaminetetraacetic acid (EDTA); 1 mmol/L ethylene glycol tetraacetic acid (EGTA); 1% Triton X-100; and 0.5% NP-40). Equal amounts of quantified protein extracts, derived from whole cell lysates,

were introduced to the m^7GTP agarose beads. The samples were then incubated with the beads on a rotator at 4°C overnight. The association of the putative proteins with the m^7G cap was assessed using Western blot analysis.

IF staining

Cells were cultured in confocal dishes for 24 hours. Cells were then fixed with 4% paraformaldehyde (Beyotime) for 15 minutes at room temperature and permeabilized with 0.5% TritonX-100 for 15 minutes at room temperature. After blocking with 5% BSA (Sigma-Aldrich) for 1 hour at room temperature, cells were incubated with primary antibody overnight at 4°C. Cells were then incubated with the following secondary antibodies for 1 hour at room temperature: CoraLite488 (SA00013-2, Proteintech) or CoraLite594 (SA00013-3, Proteintech). Images were acquired using an OLYMPUS FV1000 confocal microscopy.

IHC

For IHC staining, paraffin-embedded tissues were deparaffinized and rehydrated, and they were then subjected to antigen retrieval (ZLI-9079, ZSGB-BIO), endogenous peroxidases blocking (PV-6001, ZSGB-BIO), blocking (ZLI-9056, ZSGB-BIO), antibody incubation and staining (ZLI-9017, ZSGB-BIO). The staining index (SI) was evaluated by two independent pathologists. The staining intensity was defined as follows: negative = 0, weak = 1, intermediate = 2, and strong = 3. The proportion of positive cells was defined as follows: <5% = 0, 5%–25% = 1, 26%–50% = 2, 51%–75% = 3, and 76%–100% = 4. The SI was calculated as follows: SI = (staining intensity) (0–3) × (proportion of positive cells) (0–4).

Multiple IF analysis

For multiple-color staining, an Opal 5-color IHC kit was used according to the manufacturer's instructions. Paraffin-embedded samples were sequentially stained with primary antibodies and horseradish peroxidase–conjugated secondary antibodies. One of the four Opal reagents was used for staining, followed by microwave treatment and another round of staining. The dyes Opal520, Opal570, Opal650, Opal700, and DAPI were used for staining. Samples were visualized using the Vectra Polaris Automated Quantitative Pathology Imaging System (Perkin-Elmer). All slides were scanned at an absolute magnification of ×20 (resolution of 0.5 μm per pixel). Digital image analysis of the whole slide images was performed using HALO (RRID:SCR_018350) version 3.2.1851. Cancer-specific artificial intelligence (AI) tissue classifiers were trained using the HALO AI module to segment the tumor center, invasion margin, stroma, and background (consisting of necrosis, artifacts, and glass). The density (number of positive cells per mm^2) of positive cells on the slides was calculated.

Flow cytometry

Tumor cell digestion was performed as previously described for the isolation of primary RCC cells. After filtering, tumor cells were resuspended in PBS containing 5×10^{-3} mol/L EDTA and 1% FBS. Non-immune cells were removed via density gradient centrifugation, and the remaining cells were stained with cytometry antibodies or isotype-control antibodies. Afterward, three washes were done with PBS. For detection of cytotoxic cytokines production, cells were treated with 50 ng/mL PMA, 1×10^{-6} mol/L ionomycin, and protein transport inhibitor (BD) for 6 hours at 37°C. Cells were then fixed and permeabilized with a Fixation and Permeabilization Solution Kit (BD, 554714) following the manufacturer's instructions, and cells were then stained with the indicated primary antibodies. For measurement of HLA-A2 expression, tumor cells were stained with FITC anti-human HLA-A2 (343303, BioLegend) or isotype-control antibodies. For apoptosis analysis, cells were collected and evaluated by the Annexin V-APC/propidium iodide (PI) apoptosis kit (AP-107, Multi Science) according to the manufacturer's instructions. Samples were analyzed with a Beckman CytoFLEX Flow cytometer (Beckman Coulter, RRID:SCR_019627), and FlowJo (RRID:SCR_008520) 10 software was used to analyze the data.

RNA sequencing analysis

Total RNA was extracted using TRIzol (Invitrogen) according to the manufacturer's instructions. The mRNA was enriched by removing rRNA, digested and reverse transcribed into second-strand complementary DNA (cDNA). The cDNA library construction and sequencing were performed by Tsingke Biotechnology. The high-quality raw sequencing reads were mapped to the human reference genome (GRCh38) using the Hisat2 (RRID:SCR_015530) alignment tool. The gene expression level was normalized by fragments per kilobase of transcript per million mapped reads (FPKM). DESeq2 (RRID:SCR_015687) was used to identify differentially expressed genes (DEG).

Generation of DCs and tumor-specific $CD8^+$ T cells

For the generation of DCs, mononuclear cells were obtained from the peripheral blood of HLA-A2+ healthy donors and cultured in VIVO medium (04-418Q, Lonza) supplemented with 100 ng/mL GMCSF and 30 ng/mL IL4 (PeproTech). The medium and cytokines were replaced every 3 days. At day 6, DCs were mature, and they were stimulated with 10 ng/mL TNFα (PeproTech) for 24 hours. The DCs were then pulsed for another 24 hours with tumor lysates from HLA-A2+ patients by freeze-thawing with liquid nitrogen. To generate tumor-specific $CD8^+$ T cells, $CD8^+$ T cells were isolated from the peripheral blood of the same donors as described above. The isolated $CD8^+$ T cells were cocultured with mature DCs at a ratio of 5: 1 in VIVO medium (Lonza) containing 25 IU/mL IL2 (PeproTech) for 6 days to induce tumor-specific T cells.

Cytotoxicity assays

Tumor-specific $CD8^+$ T cells were generated as described above and cocultured with HLA-A2+ primary kidney tumor cells at an effector/target ratio of 10: 1 in 48-well plates for 12 hours at 37°C. Tumor cells were then stained with PI (ST511, Beyotime) and immediately analyzed by flow cytometry. T cells were collected and then treated with protein transport inhibitor (BD) for 6 hours at 37°C followed by fixation and permeabilization using a Fixation and Permeabilization Solution Kit (554714, BD) according to the manufacturer's instructions. Cells were then stained with PE anti-human IFNγ antibody (502508, BioLegend). Samples were analyzed with a Beckman CytoFLEX Flow cytometer (Beckman Coulter), and FlowJo 10 software was used to analyze the data.

In vivo mouse experiments

The *in vivo* mouse experiments were approved by the Institutional Animal Care and Use of Sun Yat-sen University Cancer Center (approval number 22080B) and performed in accordance with the guidelines for the care and use of animals. Six to 8 weeks old male BALB/c mice (RRID:IMSR_GPT:N000020), BALB/-Nu mice (RRID:IMSR_TAC:balbnu), or NCG (NOD/ShiLtJGptPrkdcem26Cd52Il2rgem26Cd22/Gpt) mice (IMSR, catalog no. GPT_T001475, RRID:

IMSR_GPT: T001475) were purchased from GemPharmatech and fed in standard pathogen-free conditions. BALB/c mice and BALB/-Nu mice were subcutaneously injected with stably transfected Renca cells (5×10^5cells/100 μL). The palpable tumor weight was measured every day.

For the PDX models, fragments of fresh human RCC tumors were subcutaneously transplanted into NCG mice. When the tumor volume reached 100 mm^3, the NCG mice were sacrificed. The tumors were separated and cut into 1 mm^3 pieces. Tumor pieces were transplanted into the next-generation NCG mice. After three passages, a stable RCC PDX model was successfully established. When the tumor volume reached 100 mm^3, NCG mice were randomly divided into the following five groups: control group, immune reconstitution group, immune reconstitution +siPABPC1L treatment group, immune reconstitution +αPD-1 treatment group, and immune reconstitution +siPABPC1L+αPD-1 treatment group. For adoptive T-cell transfer, tumor-specific $CD8^+$ T cells, Tregs, and DCs were injected via tail vein to rebuild the human immune system. Mice were then administered PABPC1L-siRNA (PABPC1L) or negative siRNA control (RiboBio) via intratumor injection (5 nmol every 4 days for a total of six times). For anti-PD-1 treatment, mice were intraperitoneally injected with anti-PD-1 antibody (BioXcell; 100 μg per mouse every 4 days for a total of seven times). The palpable tumor weight was measured every week. The tumor volume (mm^3) was calculated as follows: tumor volume = (length × $width^2$)/2. The mice were sacrificed when the tumor size reached 1,500 mm^3 or ulceration occurred. The tumors were separated surgically for IHC staining.

For the orthotopic xenograft models, 6 to 8 weeks old male BALB/c mice and BALB/-Nu mice were anesthetized with 1% pentobarbital (50 mg/kg) by intraperitoneal injection. Stably transfected Renca cells (5×10^5cells/25 μL) were orthotopically injected into the subcapsular of the kidney. The survival of mice was recorded.

Single-cell sequencing data processing

We employed the Seurat package (version 4.2.0, RRID:SCR_016341) for the analysis of single-cell RNA sequencing (scRNA-seq) data. Initially, 22 Seurat Objects were generated utilizing individual RCC sample gene expression matrices within Seurat. Subsequently, these Seurat Objects were filtered to exclude cells presenting with fewer than 200 genes, more than 4,500 genes, over 25% mitochondrial genes, and exceeding 1% hemoglobin genes. We then merged all Seurat Objects to create a combined Seurat Object, which was independently normalized and scaled using the NormalizeData and ScaleData functions. The Find Variable Features function was employed to identify variable genes, with 2,000 variable genes selected for downstream analysis. We conducted principal component analysis (PCA) by applying the RunPCA function. Following PCA, the RunHarmony function of the Harmony package (version 0.1.1, RRID:SCR_022206) was utilized for Seurat Object integration and batch effect correction across various samples. Ultimately, clustering was performed using the Find Neighbors and Find Clusters functions, employing 50 principal components for analysis. The Uniform Manifold Approximation and Projection (UMAP) method was then applied to visualize the cell atlas.

We identified distinct genes within cell clusters using the Find All Markers function via Wilcoxon rank-sum tests. Each cell cluster was subsequently classified as a specific cell type based on classical marker genes as delineated below: RCCs (marked by CA9 and NDUFA4L2), T cells (marked by CD3D and CD3E), $CD8^+$ T cells (marked by CD8A and CD8B), helper T cells (marked by CD4 and CD40LG), Tregs (marked by FOXP3), natural killer cells (NK cells, marked by NKG7 and GNLY), B cells (marked by CD79A and MS4A1), plasma cells (marked by JCHAIN and MZB1), monocytes (marked by CD14 and S100A8), macrophages (marked by CD68, C1QA, and C1QB), conventional dendritic cells (cDC, marked by CD1C), plasmacytoid dendritic cells (pDC, marked by LILRA4), mast cells (marked by CPA3 and KIT), vascular smooth muscle cells (marked by ACTA2, ATAC2, and MYH11), ascending vasa recta cells (marked by FXYD2, FXYD6, and IGFBP7), and pericytes (marked by RGS5 and PDGFRB).

We extracted immune cell data (T cells, NK cells, B cells, plasma cells, monocytes, macrophages, cDCs, pDCs, and mast cells) from the integrated scRNA-seq dataset. The Harmony package was then employed to integrate the scRNA-seq data of immune cells. The immune cell atlas visualization was implemented using the UMAP method for further analyses. $CD8^+$ T cells were extracted and visualized from the immune cell atlas to explore the functional changes of $CD8^+$ T cells further. For trajectory analysis of the $CD8^+$ T-cell atlas, the Monocle3 R package (RRID:SCR_018685) was utilized to conduct pseudotime ordering and infer the state evolution process of $CD8^+$ T cells.

ELISA

Blood samples were collected using a serum separator tube from mice before euthanasia. Then, samples were allowed to clot at room temperature for 1 hour followed by centrifugation for 10 minutes at 3,000 × *g*. Serum was then transferred to a new tube and stored at −80°C before analysis. For coculture assays, supernatant from primary kidney tumor cells cocultured with tumor specific $CD8^+$ T cells was collected and stored at −80°C. IFNγ levels in the serum samples were measured with a human IFNγ ELISA kit (Elikine).

The detection assays of TRP-associated metabolites

The detection of TRP-associated metabolites has been described previously (11). Cell cultures were grown in 100 mm dishes at a density of 2×10^6 cells per dish. Following incubation, supernatants were harvested, and any detached cells were eliminated via filtration through a 0.45 mm filter. Quantification of KYN and TRP levels within these supernatants was conducted using an ELISA kit specifically designed to measure the KYN/TRP ratio (ISE-2227; ImmuSmol), adhering strictly to the protocol provided by the kit manufacturer. Concentrations of TRP and KYN were deduced by comparison with the kit's provided standards, and from these, the KYN/TRP ratio was calculated. In the analysis of mouse plasma, 100 ± 5 μL samples of thawed mouse plasma were transferred to 2 mL centrifuge tubes. To each sample, 10 μL of an internal standard and 0.4 mL of an acetonitrile-methanol mixture were added, followed by thorough vortex mixing. Samples were then centrifuged at 14,000 × *g*, and 400 μL of the supernatant was drawn off and evaporated under nitrogen gas. The dry residue was reconstituted in 100 μL of an acetonitrile-water mixture and centrifuged once more at 14,000 × *g* to clarify. The final supernatant was subjected to high-performance liquid chromatography-tandem mass spectrometry (HPLC/MS-MS) analysis, conducted by Applied Protein Technology Company. Data quantitation was performed using either MultiQuant or Analyst software, with manual verification of peak integration.

Luciferase assays

A series of reporter plasmids was transfected into 769-P and 786-O cells using Lipofectamine 3000 reagent (L3000015, Invitrogen) according to the manufacturer's recommendations. Luciferase signals were

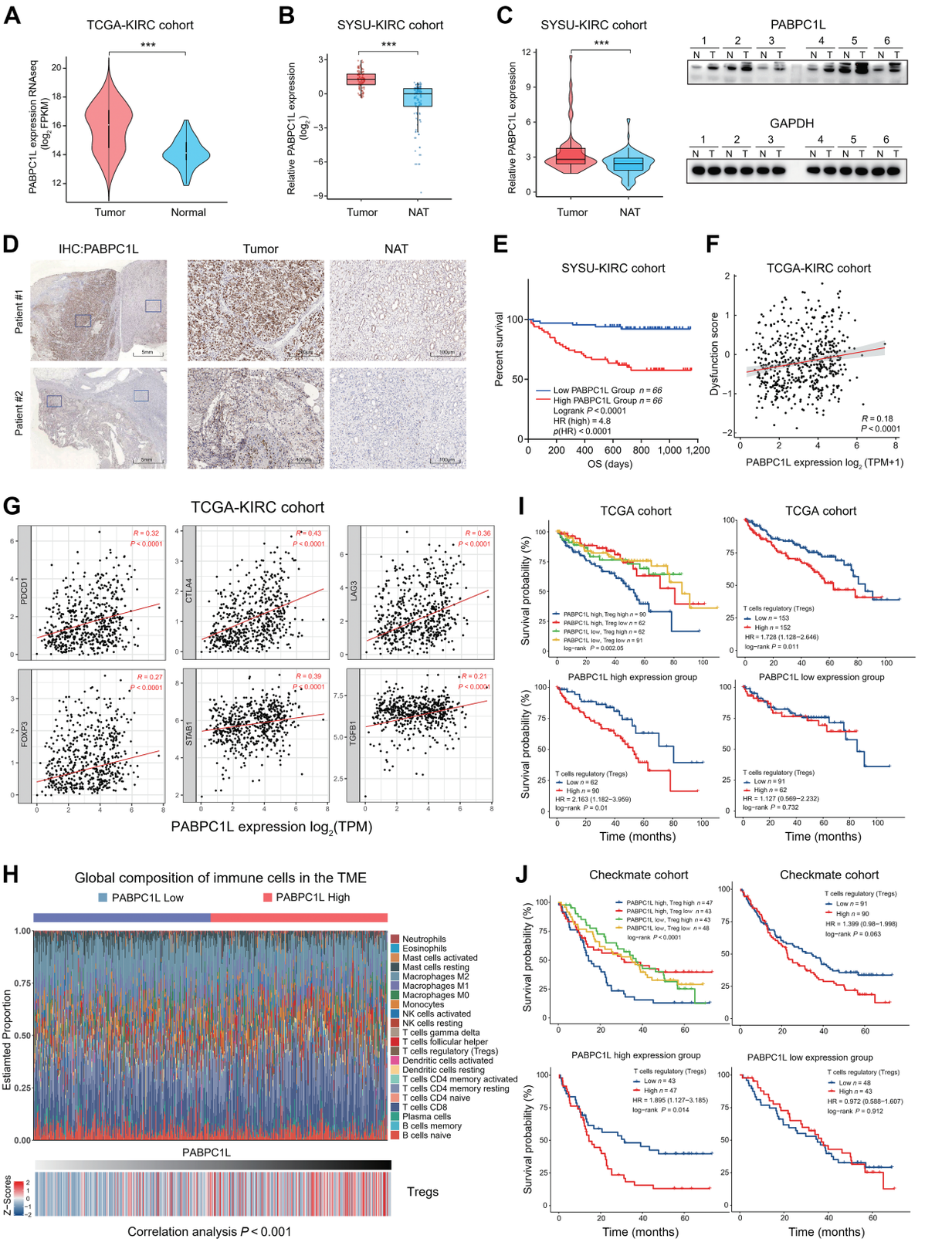
A
TCGA-KIRC cohort
***
PABPC1L expression RNAseq (log2 FPKM)
Tumor
Normal
B
SYSU-KIRC cohort
***
Relative PABPC1L expression (log2)
Tumor
NAT
C
SYSU-KIRC cohort
***
Relative PABPC1L expression
Tumor
NAT
PABPC1L
GAPDH
N T N T N T N T N T N T
D
IHC:PABPC1L
Tumor
NAT
Patient #1
Patient #2
E
SYSU-KIRC cohort
Percent survival
Low PABPC1L Group n = 66
High PABPC1L Group n = 66
Logrank P < 0.0001
HR (high) = 4.8
p(HR) < 0.0001
OS (days)
F
TCGA-KIRC cohort
Dysfunction score
R = 0.18
P < 0.0001
PABPC1L expression log2 (TPM+1)
G
TCGA-KIRC cohort
PDCD1
CTLA4
LAG3
FOXP3
STAB1
TGFB1
PABPC1L expression log2(TPM)
I
TCGA cohort
Survival probability (%)
PABPC1L high, Treg high n = 90
PABPC1L high, Treg low n = 62
PABPC1L low, Treg high n = 62
PABPC1L low, Treg low n = 91
log-rank P = 0.002.05
T cells regulatory (Tregs)
Low n = 153
High n = 152
HR = 1.728 (1.128−2.646)
log-rank P = 0.011
PABPC1L high expression group
PABPC1L low expression group
T cells regulatory (Tregs)
Low n = 62
High n = 90
HR = 2.163 (1.182−3.959)
log-rank P = 0.01
Low n = 91
High n = 62
HR = 1.127 (0.569−2.232)
log-rank P = 0.732
Time (months)
H
Global composition of immune cells in the TME
PABPC1L Low
PABPC1L High
Estiamted Proportion
Neutrophils
Eosinophils
Mast cells activated
Mast cells resting
Macrophages M2
Macrophages M1
Macrophages M0
Monocytes
NK cells activated
NK cells resting
T cells gamma delta
T cells follicular helper
T cells regulatory (Tregs)
Dendritic cells activated
Dendritic cells resting
T cells CD4 memory activated
T cells CD4 memory resting
T cells CD4 naive
T cells CD8
Plasma cells
B cells memory
B cells naive
PABPC1L
Z-Scores
Tregs
Correlation analysis P < 0.001
J
Checkmate cohort
PABPC1L high, Treg high n = 47
PABPC1L high, Treg low n = 43
PABPC1L low, Treg high n = 43
PABPC1L low, Treg low n = 48
log-rank P < 0.0001
T cells regulatory (Tregs)
Low n = 91
High n = 90
HR = 1.399 (0.98−1.998)
log-rank P = 0.063
PABPC1L high expression group
PABPC1L low expression group
Low n = 43
High n = 47
HR = 1.895 (1.127−3.185)
log-rank P = 0.014
Low n = 48
High n = 43
HR = 0.972 (0.588−1.607)
log-rank P = 0.912
Survival probability (%)
Time (months)

measured using the Dual Luciferase Reporter Assay Kit (E1960, Promega).

T-cell suppression assay

Unstimulated T cells were used as a negative control. Naïve $CD8^+$ T were isolated using a mouse Spleen Dissociation Kit (130-095-926, Miltenyi Biotec) and mouse CD8a (Ly-2) MicroBeads (130-117-044, Miltenyi Biotec). $CD8^+$ T cells were used immediately after isolation. Naïve $CD8^+$ T cells were stained with 5 mmol/L of carboxyfluorescein succinimidyl ester (CFSE) by incubation at room temperature for 5 minutes in the dark. The CFSE surplus was removed by two washing steps with 1×PBS. Enriched naïve $CD8^+$ T cells (1×10^5) were stimulated in U-bottomed 96-well plates that were precoated with 2 μg/mL anti-CD3 (130-097-621, Miltenyi Biotec) and anti-CD28 (130-093-182, Miltenyi Biotec). After being stimulated for 48 hours, the cells were transferred to new wells and rested for 24 hours. For the conditioned medium, tumor cells were seeded at a density of 50,000 cells/cm^2 and cultured in the presence or absence of KYNU (1 μmol/L) or vehicle control (10% DMSO in PBS) for 48 hours. Supernatants of each group of tumor cells were centrifuged at 1,000 × *g* for 5 minutes. The CFSE-labeled $CD8^+$ T cells were exposed to a conditioned medium or media supplemented with 5% FBS. Then, the $CD8^+$ T cells were collected, washed twice in 1×PBS, and resuspended in 500 μL of 1×PBS before analysis by flow cytometry. Unstimulated T cells were used as a negative control.

Immunoprecipitation of RNA-binding proteins

RNA immunoprecipitation (RIP) was carried out using an EZ-Magna RIP Kit (Millipore) according to the manufacturer's instructions. The bounded proteins were further confirmed by Western blotting. The immunoprecipitated RNA was subjected to qRT-PCR analysis.

RIP sequencing experiment

Following the extraction of total RNA, rRNAs were selectively depleted, preserving mRNAs and noncoding RNAs (ncRNA). This RNA pool was subsequently fragmented into smaller pieces using a specialized fragmentation buffer, and then reverse transcribed into cDNA utilizing random primers. The synthesis of the second-strand cDNA was facilitated by employing DNA Polymerase I, RNase H, a dNTP mix (substituting dTTP with dUTP), and a reaction buffer. The resulting cDNA fragments underwent purification using the QiaQuick PCR Purification Kit, followed by end repair, polyadenylation, and adapter ligation with Illumina sequencing adapters. Post-adapter ligation, Uracil-N-Glycosylase (UNG) was applied to remove the uracil-containing second-strand cDNA, ensuring strand specificity. The prepared samples were then subjected to size selection via agarose gel electrophoresis, PCR enrichment, and finally sequenced on an Illumina HiSeq 4000 system by Gene Denovo Biotechnology Co. To get high-quality clean reads, reads were further filtered according to the following rules: (i) Removing reads containing adapters; (ii) Removing reads containing more than10% of unknown nucleotides(N); (iii) Removing low quality reads containing more than 50% of low-quality (Q value ≤20) bases. Short reads alignment tool Bowtie2 (2.2.8) was used for mapping reads to rRNA database. The rRNA mapped reads were then removed. The remaining reads were further used in assembly and analysis of transcriptome. The rRNA removed reads of each sample were then mapped to reference genome by TopHat2 (version 2.1.1), respectively. After aligned with reference genome, unmapped reads (or mapped very poorly) were then re-aligned with Bowtie2, the enriched unmapped reads were split into smaller segments which were then used to find potential splice sites. The section and the section position of these short segments were predicted as well. The reconstruction of transcripts was carried out with software StringTie, which allows to identify splice variants. During the last step of assembly, all of the reassembles fragments were aligned with reference genes and then similar fragments were removed. To identify regions of IP enrichment over background, we used the RIPSeeker algorithm, which is a *de novo* method for detecting peaks (indicating protein–RNA interactions) based on hidden Markov models. eFDR<0.05 and IP count>10 was used to select peaks. Then, the information of genomic location, fold enrichment, and significant level of peaks were all displayed. According to the genomic location information and gene annotation information of peak, peak-related genes can be confirmed. Besides, the distribution of peak on different function regions, such as protein coding, pseudogene and antisense, was performed.

Actinomycin D treatment

When at 60% confluency in 6-well plates, cells were treated with 5 μg/mL actinomycin D or DMSO and harvested at specific time-points. Afterward, expression levels of mRNAs were quantified through qRT-PCR.

Chromatin immunoprecipitation assay

The chromatin immunoprecipitation (ChIP) assay was performed using SimpleChIP Plus Enzymatic Chromatin IP Kit (CST). Briefly, cell samples went through cross-linking, chromatin digestion, elution of chromatin and reversal of cross-links, DNA purification, and qPCR. Anti-STAT1 antibodies and normal Rabbit IgG were used in this assay.

Polysome analysis

Polysome analysis was conducted as our described previously (26). Prior to cell lysis, around 1.5×10^7 cells underwent incubation in a complete medium supplemented with 100 mg/mL cycloheximide (CHX) at 37°C for a duration of 10 minutes. Subsequently, the cells were gathered and subjected to centrifugation at 1,000 × *g* for 5 minutes at 4°C. The supernatant was discarded, and 500 mL of lysis

Figure 1.
PABPC1L is upregulated in RCC and is correlated with immunosuppression in RCC. **A,** *PABPC1L* mRNA levels in RCC tumor tissues and normal tissues from TCGA database. **B,** Relative RNA expression of *PABPC1L* in human RCC tumors (T) and matched normal adjacent tissues (NAT) according to qRT-PCR in SYSU-KIRC cohort. **C,** Representative Western blot (right) and statistical analysis (left) of PABPC1L protein expression levels in SYSU-KIRC cohort. **D,** Representative IHC images showing the expression of *PABPC1L* in tumors and matched normal adjacent tissues. **E,** OS of patients with RCC with low ($n = 66$) or high ($n = 66$) *PABPC1L* expression in SYSU-KIRC cohort. **F,** TIDE analysis revealed that *PABPC1L* was positively associated with immune dysfunction score in TCGA-KIRC dataset. **G,** *PABPC1L* was positively associated with inhibitory checkpoints, Treg marker and M2 tumor-associated macrophage markers according to TCGA database. **H,** *PABPC1L* expression group and proportions of TME cells for 305 patients in TCGA-KIRC cohort and the elevated infiltration level of Tregs upon higher expression of *PABPC1L*. **I,** OS of patients with RCC in the TCGA-KIRC cohort, stratified by both *PABPC1L* expression and Treg infiltration. **J,** OS of patients with RCC in the Checkmate cohort, stratified by both *PABPC1L* expression and Treg infiltration. ***, $P < 0.001$.

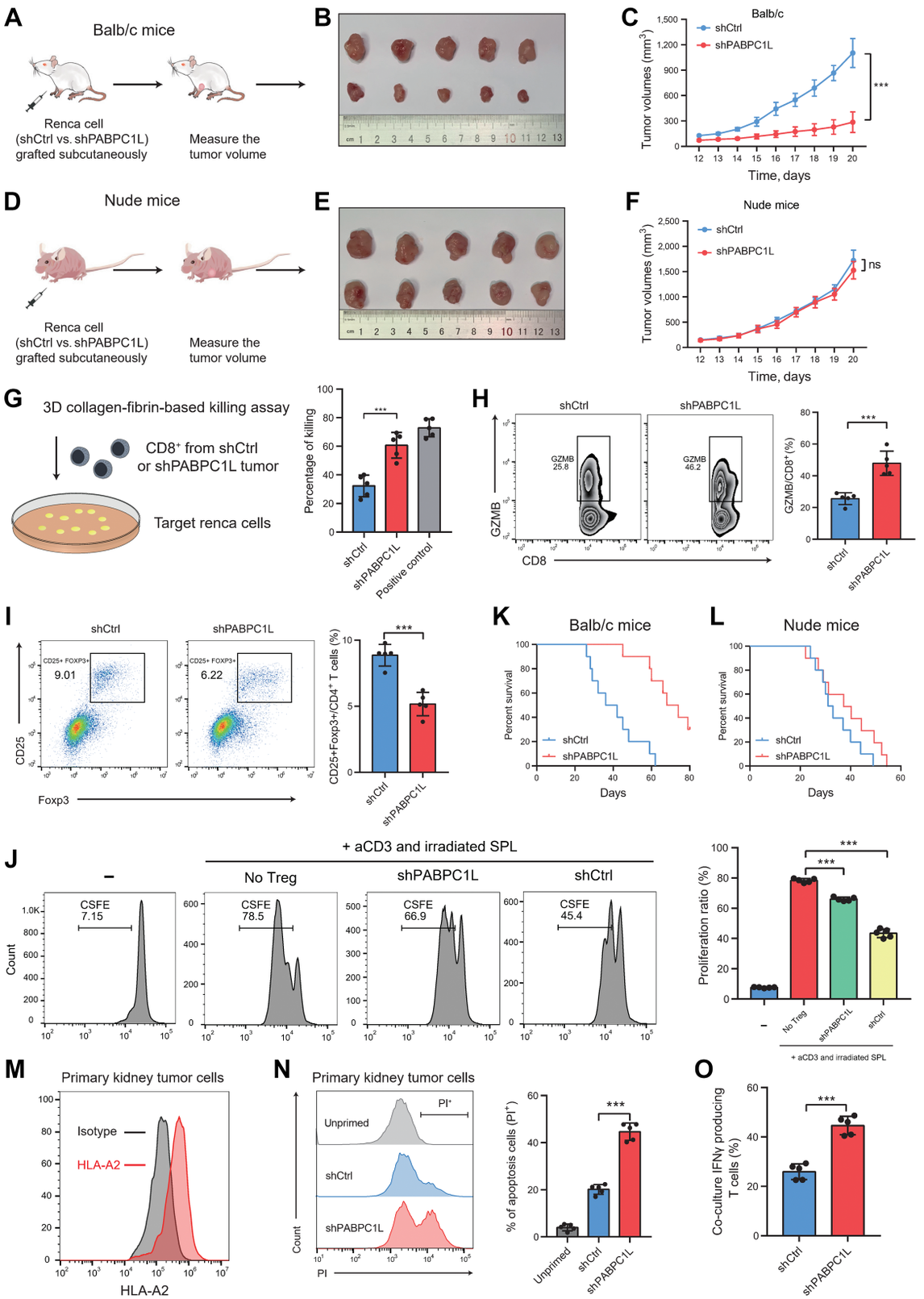
A
Balb/c mice
Renca cell
(shCtrl vs. shPABPC1L)
grafted subcutaneously
Measure the
tumor volume
B
C
Balb/c
shCtrl
shPABPC1L
Tumor volumes (mm3)
Time, days
***
D
Nude mice
Renca cell
(shCtrl vs. shPABPC1L)
grafted subcutaneously
Measure the
tumor volume
E
F
Nude mice
shCtrl
shPABPC1L
Tumor volumes (mm3)
Time, days
ns
G
3D collagen-fibrin-based killing assay
CD8+ from shCtrl
or shPABPC1L tumor
Target renca cells
Percentage of killing
shCtrl
shPABPC1L
Positive control
H
shCtrl
shPABPC1L
GZMB
25.8
GZMB
46.2
CD8
GZMB/CD8+ (%)
I
shCtrl
shPABPC1L
CD25+ FOXP3+
9.01
6.22
CD25
Foxp3
CD25+Foxp3+/CD4+ T cells (%)
K
Balb/c mice
Percent survival
Days
shCtrl
shPABPC1L
L
Nude mice
Percent survival
Days
shCtrl
shPABPC1L
J
+ aCD3 and irradiated SPL
–
No Treg
shPABPC1L
shCtrl
CSFE
7.15
CSFE
78.5
CSFE
66.9
CSFE
45.4
Count
Proliferation ratio (%)
M
Primary kidney tumor cells
Isotype
HLA-A2
HLA-A2
N
Primary kidney tumor cells
Unprimed
shCtrl
shPABPC1L
PI+
Count
PI
% of apoptosis cells (PI+)
Unprimed
shCtrl
shPABPC1L
O
Co-culture IFNγ producing
T cells (%)
shCtrl
shPABPC1L

buffer [containing 300 mmol/L NaCl, 20 mmol/L Tris-HCl at pH 7.4, 10 mmol/L $MgCl_2$, 1% Triton X-100, 1 mmol/L 1,4-dithiothreitol, 100 mg/mL CHX, 0.5% sodium deoxycholate (w/v), an EDTA-free protease inhibitor mix, and an RNase inhibitor] was added to each sample, which was then chilled on ice for 10 minutes. Following this, the samples were centrifuged at 13,000 × *g* for 5 minutes at 4°C to separate the lysis products, and the supernatants were retained for RNA concentration measurements. Sucrose gradients were prepared using 5% and 50% sucrose solutions, each containing 100 mg/mL CHX, using a Gradient Master 108 (Biocomp). Samples of equalized cell extracts were layered onto these gradients in ultracentrifuge tubes (Beckman Coulter) and centrifuged using a SW41 rotor in a Beckman Coulter Optima L-100XP ultracentrifuge at 39,000 rpm for 120 minutes at 4°C. Postcentrifugation, 12 fractions were meticulously collected from each tube with a Piston Gradient Fractinator (Biocomp). RNA was then isolated from each fraction using TRIzol reagent (Invitrogen), followed by reverse transcription. qRT-PCR analyses were conducted to examine the RNA profiles.

Bioinformatics analysis

The clinical data and RNA sequencing (RNA-seq) data of The Cancer Genome Atlas (TCGA)-Kidney Renal Clear Cell Carcinoma (KIRC) cohort were downloaded from Firebrowse (http://firebrowse.org/). The tumor immune infiltration analyses were performed using the CIBERSORT algorithm (https://cibersortx.stanford.edu/), samples with a *P* value less than 0.05 were included in the subsequent analysis. Gene set enrichment analysis (GSEA) was performed using GSEA software version 4.1.0 (Broad Institute). T-cell dysfunction analyses were performed using TIDE tools (http://tide.dfci.harvard.edu/).

Statistical analyses

Statistical analyses were performed using SPSS (RRID: SCR_002865) version 22.0 or GraphPad Prism (RRID:SCR_002798) software. Data are presented as the mean ± SD. All *in vitro* experiments were performed with at least three independent biological replicates. Data were analyzed for normality before comparisons. For comparisons between two groups, statistical significance was determined by two-tailed Student *t* test. For multiple comparisons, one-way ANOVA with Tukey *post hoc* test was used. For the survival analyses, overall survival (OS) was defined as the time from the operation to the date of death for any reason. Kaplan–Meier survival curves were plotted with log-rank tests. Correlation analyses were performed using Pearson correlation (continuous variables) or Spearman correlation (discontinuous variables). *P* value less than 0.05 was considered significant. Statistical significance was shown as *, $P < 0.05$; **, $P < 0.01$; or ***, $P < 0.001$.

Data availability statement

The scRNA-seq data analyzed in this study were obtained from National Center for Biotechnology Information Gene Expression Omnibus at GSE159115 (https://www.ncbi.nlm.nih.gov/geo/query/acc.cgi?acc=GSE159115) and dbGaP at phs002252.v1.p1. Bulk RNA-seq and clinical data for TCGA-KIRC cohort were obtained from The NCI's Genomic Data Commons at https://gdc.cancer.gov/about-data/publications/pancanatlas. Bulk RNA-seq and clinical data for CheckMate cohorts were obtained from European Genome-phenome Archive at EGAS00001004290, EGAS00001004291, and EGAS00001004290. The data generated in this study are publicly available in Gene Expression Omnibus at GSE241871 and GSE255448. All other raw data are available upon request from the corresponding author.

Results

PABPC1L is a prognostic factor and associated with immunosuppression in RCC

In our previous study, we identified *PABPC1L* as a hypoxia-immune biomarker for RCC (23). To further elucidate the potential role of *PABPC1L* in RCC, we evaluated the expression levels of *PABPC1L* in both tumor and normal tissues utilizing TCGA database. Comprehensive bioinformatics analyses indicated that *PABPC1L* was significantly upregulated in multiple cancer types, including KIRC (**Fig. 1A**; Supplementary Fig. S1A). The increased expression of *PABPC1L* in tumor tissues relative to normal adjacent tissue was subsequently corroborated through qPCR, Western blotting, and IHC staining (**Fig. 1B–D**). Kaplan–Meier survival analyses demonstrated a significant correlation between elevated *PABPC1L* expression and reduced OS in patients with RCC within both TCGA-KIRC cohort and Checkmate cohort (Supplementary Fig. S1B and S1C). This finding was further corroborated in an independent RCC cohort obtained from SYSU, where *PABPC1L* expression was assessed through IHC staining (**Fig. 1E**).

To examine the detailed role of *PABPC1L* in RCC, we investigated the RNA expression profiles derived from TCGA-KIRC database. In alignment with our previous study (23), the current analysis substantiated that *PABPC1L* expression was positively correlated with immune dysfunction scores, as computed utilizing the Tumor Immune Dysfunction and Exclusion (TIDE) algorithm (**Fig. 1F**). Moreover, there is a positive correlation between *PABPC1L* and inhibitory checkpoints (*PDCD1*, *CTLA4*, *LAG3*), Treg marker (*FOXP3*) and M2 tumor-associated macrophage markers (*STAB1*, *TGFB1*) according to TCGA database (**Fig. 1G**). Intriguingly, while *PABPC1L* expression did not induce a comprehensive alteration in the

Figure 2.

PABPC1L deficiency improves antitumor immunity in murine and human RCC. **A** and **D,** Schematic of Renca cells with/without *PABPC1L* knockdown subcutaneously injected into BALB/c (**A**) and nude (**D**) mice. **B** and **C,** Images of tumors (**B**) and growth curves (**C**) in BALB/c mice ($n = 5$/group). **E** and **F,** Tumor images (**E**) and growth curves (**F**) in nude mice ($n = 5$/group). **G,** Schematic of the experimental setup for the 3D collagen-fibrin gel killing assay (left) and quantification of target cell killing by tumor-isolated $CD8^+$ T cells or tumor antigen–specific $CD8^+$ T cells (right). **H,** Flow cytometry analysis of GZMB in $CD8^+$ T cells isolated from indicated Renca tumors in BALB/c mice. **I,** Flow cytometric analysis of Foxp3 expression in tumor-infiltrating $CD4^+$ populations isolated from indicated Renca tumors in BALB/c mice. **J,** *In vitro* suppressive activity of tumor-isolated Tregs isolated from shPABPC1L or shCtrl mice. Left, representative histograms of $CD8^+$ T-cell proliferation. Right, FACS quantification of T-cell proliferation. **K** and **L,** Survival curves of BALB/c (**K**) and nude (**L**) mice with Renca cells ($n = 10$/group). **M,** Flow cytometry analysis of HLA-A2 expression in primary kidney tumor cells. **N,** Representative flow cytometry histograms (left) and statistical analysis (right) of apoptosis rate (PI+) of primary kidney tumor cells with or without *PABPC1L* knockdown cocultured with primary kidney tumor-specific $CD8^+$ T cells. **O,** The proportion of IFNγ-producing T cells in shPABPC1L or shCtrl samples. **A–F,** Data represent one independent experiment with 5 mice per group. **G,** Data are representative of five independent experiments. **H–J,** Each experiment was repeated three times with 5 mice per group, and data shown are the representative group of three independent experiments. **K** and **L**, Data represent one independent experiment with 10 mice per group. **N** and **O**, Data represent five independent biological replicates. ***, $P < 0.001$.

immune cell composition within the TME (**Fig. 1H**), infiltration level of Tregs was elevated upon higher expression of *PABPC1L* (**Fig. 1H**). Consequently, we postulated that *PABPC1L* might facilitate the infiltration of Tregs, thereby suppressing the cytotoxicity of T cells and ultimately inducing tumor immune evasion.

In light of the crucial function of Tregs in modulating antitumor immune responses, which affect patient prognosis, we proceeded to examine the prognostic relevance of *PABPC1L* and Tregs infiltration, as determined by the Cibersort algorithm, within TCGA KIRC cohort. In accordance with our hypothesis, Tregs infiltration emerged as a risk factor for patient survival. Patients exhibiting elevated *PABPC1L* expression in conjunction with high Tregs infiltration demonstrated the most unfavorable survival outcomes (**Fig. 1I**). Remarkably, in contrast to the high *PABPC1L* expression group, low *PABPC1L* expression effectively abolished the survival risk associated with Tregs infiltration (**Fig. 1I**). In addition, within the Checkmate cohort, in which patients with metastatic RCC receiving ICB therapy, we observed that the correlation between high Tregs infiltration and poor OS was abrogated, likely due to the ICB treatment. However, in the subset of patients with elevated *PABPC1L* expression, Tregs infiltration once again emerged as a risk factor for survival (**Fig. 1J**). Therefore, high *PABPC1L* expression seems to be critical for Tregs to suppress antitumor immune responses, which affect patient prognosis. Collectively, our findings suggest that increased *PABPC1L* expression is unfavorable for patients with RCC and may be associated with a dampened immune response, potentially attributable to Tregs.

PABPC1L depletion enhances antitumor immune response in RCC

To investigate the potential association between *PABPC1L* and antitumor immune responses, we specifically knocked down *PABPC1L* in the Renca, the murine RCC cell line using lentiviral shRNAs (Supplementary Fig. S2A). Silencing *PABPC1L* did not affect the *in vitro* proliferation of Renca cells (Supplementary Fig. S2B). Interestingly, when compared with control cells (shCtrl), *PABPC1L* knockdown (shPABPC1L) significantly impeded Renca-derived tumor growth in immunocompetent BALB/c mice (**Fig. 2A–C**), but not in immunodeficient nude mice (**Fig. 2D–F**). These findings suggested that *PABPC1L* did not affect RCC cell proliferation and primarily modulated tumor growth by mediating interactions between tumor cells and immune cells. To determine whether *PABPC1L* deletion enhances the cytotoxicity of T cells *in vivo*, we isolated $CD8^+$ T cells from the aforementioned Renca tumors in BALB/c mice using FACS and further evaluated their cytotoxic capacity in a 3D collagen-fibrin–based killing assay, as described previously (25). Analysis of the $CD8^+$ T cells' killing ability demonstrated a 32% killing efficiency for shCtrl-isolated $CD8^+$ T cells, in contrast to 61% for shPABPC1L-isolated $CD8^+$ T cells and 73% for positive control *in vitro* activated tumor antigen-specific $CD8^+$ T cells (**Fig. 2G**; Supplementary Fig. S2C). Furthermore, flow cytometry analysis indicated that the effector function of $CD8^+$ T cells (as indicated by granzyme B expression, GZMB) was enhanced in the shPABPC1L group (**Fig. 2H**). Further examination of the immune infiltrate in shPABPC1L tumors revealed a reduced frequency of Tregs within intratumoral $CD4^+$ T cells compared with shCtrl tumors (**Fig. 2I**; Supplementary Fig. S2D). Notably, Tregs isolated from shCtrl tumors demonstrated a superior capacity to suppress the proliferation of autologous $CD8^+$ T cells *in vitro* relative to shPABPC1L-isolated Tregs (**Fig. 2J**). In an orthotopic tumor model, notably enhanced survival was observed in immunocompetent mice implanted with shPABPC1L Renca cells, but not in immunodeficient nude mice (**Fig. 2K** and **L**; Supplementary Fig. S2E and S2F). Taken together, our Renca tumor model suggests that the loss of *PABPC1L* improved the antitumor immunity in murine RCC.

To investigate the role of *PABPC1L* in more clinically relevant models, primary tumor cells were isolated from patients with HLA-A2+ RCC (**Fig. 2M**). By means of activating T cells with DCs pulsed with primary tumor lysates, tumor-specific $CD8^+$ T cells were generated, as previously delineated (Supplementary Fig. S2G; refs. 27, 28). Tumor-isolated Tregs, tumor-specific $CD8^+$ T cells, and primary tumor cells were cocultured *in vitro*. Remarkably, the silencing of *PABPC1L* in primary tumor cells substantially enhanced the cytotoxicity of primary tumor antigen-activated $CD8^+$ T cells toward target tumor cells (**Fig. 2N**). In concordance with this observation, the loss of *PABPC1L* resulted in an elevation in the proportion of IFNγ-producing T cells (**Fig. 2O**). Collectively, our experiments demonstrate that high expression of *PABPC1L* in human RCC cells inhibits antitumor immune efficacy.

Expression of *PABPC1L* in RCC is associated with intratumoral Tregs infiltration and immunosuppression

To confirm the immunosuppressive function of *PABPC1L*, as suggested by clinical evidence, we conducted an integrated investigation utilizing published scRNA-seq analysis of RCC (29, 30) and constructed RCC tumor atlases with scRNA-seq data, which included 139,025 high-quality cells from 22 RCC samples. By examining RCC tumor tissues, we found that *PABPC1L* was predominantly expressed in RCC tumor cells, as opposed to other cellular components (Supplementary Fig. S3A). To further investigate the influence of *PABPC1L* on tumor immune infiltration, clinical samples from single-cell sequencing were classified according to *PABPC1L* expression levels in tumor cells, dividing them into high-expression and low-expression groups. Upon reclustering the tumor-infiltrating immune cells, we discovered that samples with elevated *PABPC1L* expression exhibited reduced infiltration of $CD8^+$ T cells and enhanced infiltration of Tregs. In contrast, samples with low *PABPC1L* expression displayed elevated $CD8^+$ T-cell infiltration levels and reduced Tregs infiltration (**Fig. 3A**). To further validate these findings, we assessed the protein levels of PABPC1L in RCC samples from our center through Western blotting (**Fig. 1C**). Moreover, we utilized multiplex IF to evaluate the infiltration levels of Tregs and $CD8^+$ T cells within patient tumor tissues. The results demonstrated that PABPC1L+ cells were predominantly overlapped with CK+ tumor cells, as opposed to $CD8^+$ or $FOXP3^+$ immune cells (**Fig. 3B**; Supplementary Fig. S3B). In tumor tissues of patients with high *PABPC1L* expression, the levels of Tregs in tertiary lymphoid structures were significantly elevated compared with those with low *PABPC1L* expression, while infiltration levels of $CD8^+$ T cells in tumorous area were notably reduced in comparison with patients with low *PABPC1L* expression (**Fig. 3C**). Furthermore, within the same tissue section, regions with high *PABPC1L* expression exhibited decreased infiltration levels of $CD8^+$ T cells, whereas the opposite pattern was observed in regions with low *PABPC1L* expression (**Fig. 3D**). Utilizing TissueFAXS Cytometry technology, we analyzed the spatial relationships and interactions between tumor cells and T cells within the tissue microenvironment. Spatial distribution scatterplots revealed that in samples with low *PABPC1L* expression, $CD8^+$ T cells were primarily located within 30 μm of tumor cells, with an extremely low number of $CD8^+$ T cells observed beyond this distance. In contrast, in samples with high *PABPC1L* expression, $CD8^+$ T cells were predominantly distributed beyond 150 μm from tumor cells. The percentage of $CD8^+$ T cells within 30 μm was significantly reduced compared with samples with low *PABPC1L* expression, while the

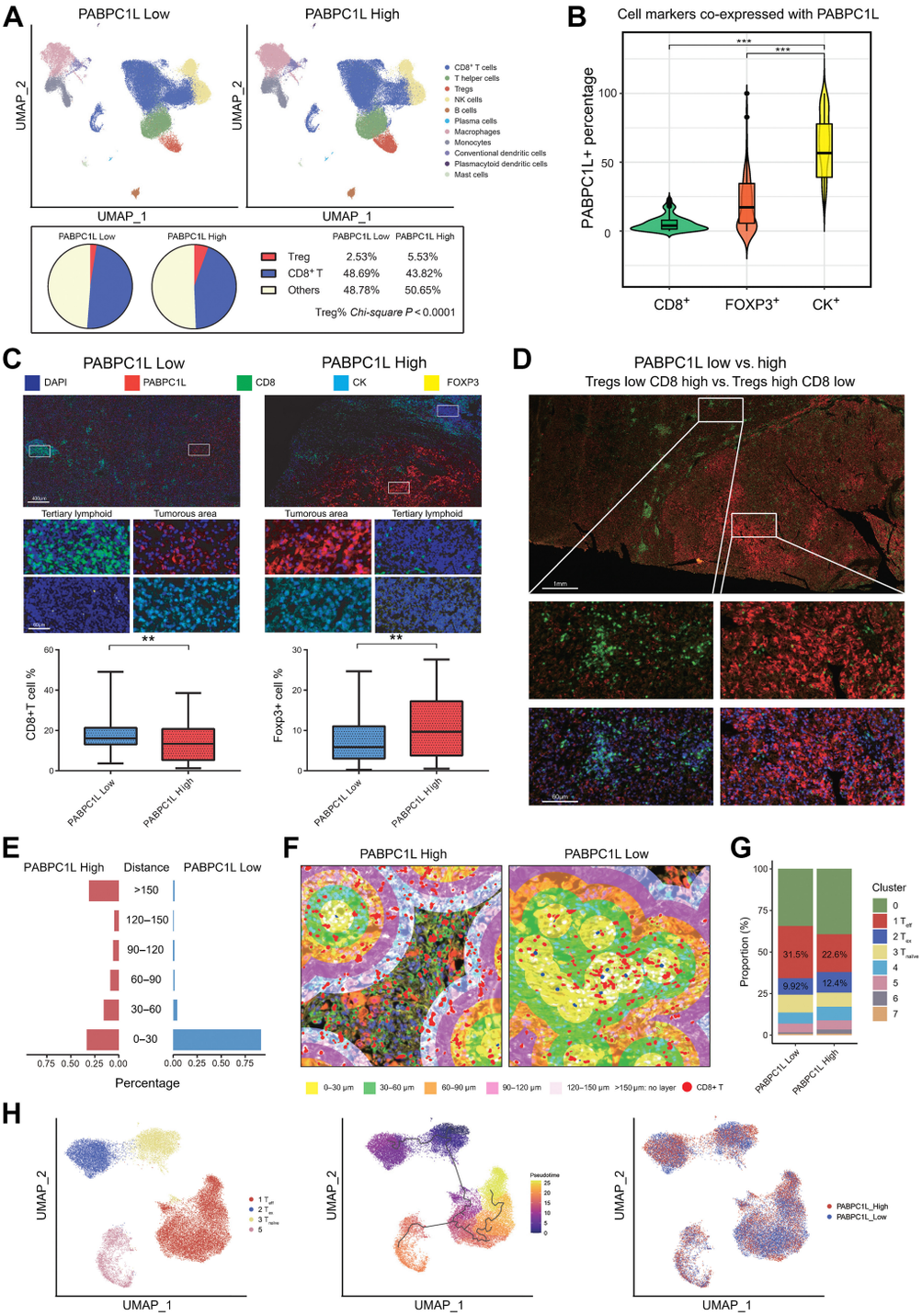

Figure 3.

Effect of RCC *PABPC1L* expression in Tregs infiltration at single-cell resolution and Tregs spatial distribution in the TME. **A,** Top, UMAP plots of tumor-infiltrating immune cells in tumor tissues with high or low expression of *PABPC1L*. Bottom, distribution of tumor-infiltrating immune cell clusters across tumor tissues with high or low expression of *PABPC1L*. **B,** Cell markers coexpressed with PABPC1L+ cells. **C,** Multiplex IF detected the infiltration levels of Tregs and $CD8^+$ T cells in tumor tissues from patients with high or low *PABPC1L* expression. Scale bars, 400 or 60 μm. **D,** The level of infiltration of $CD8^+$ T in the high expression region of *PABPC1L* was significantly different from that in the low expression region. Scale bars, 1 mm or 60 μm. **E,** Statistical analysis of $CD8^+$ T cells spatial distribution in tumor tissues with high and low expression of *PABPC1L*. **F,** Representative spatial distribution scatterplots of $CD8^+$ T cells in tumor tissues with high and low expression of *PABPC1L*. **G,** Percentage distribution of T-cell clusters in tumor tissues with high or low expression of *PABPC1L*. **H,** The potential developmental trajectory of T-cell clusters in TME. Each dot represents a single cell, colored according to clusters (left), pseudotime (middle), or *PABPC1L* expression group. **, $P < 0.01$; ***, $P < 0.001$.

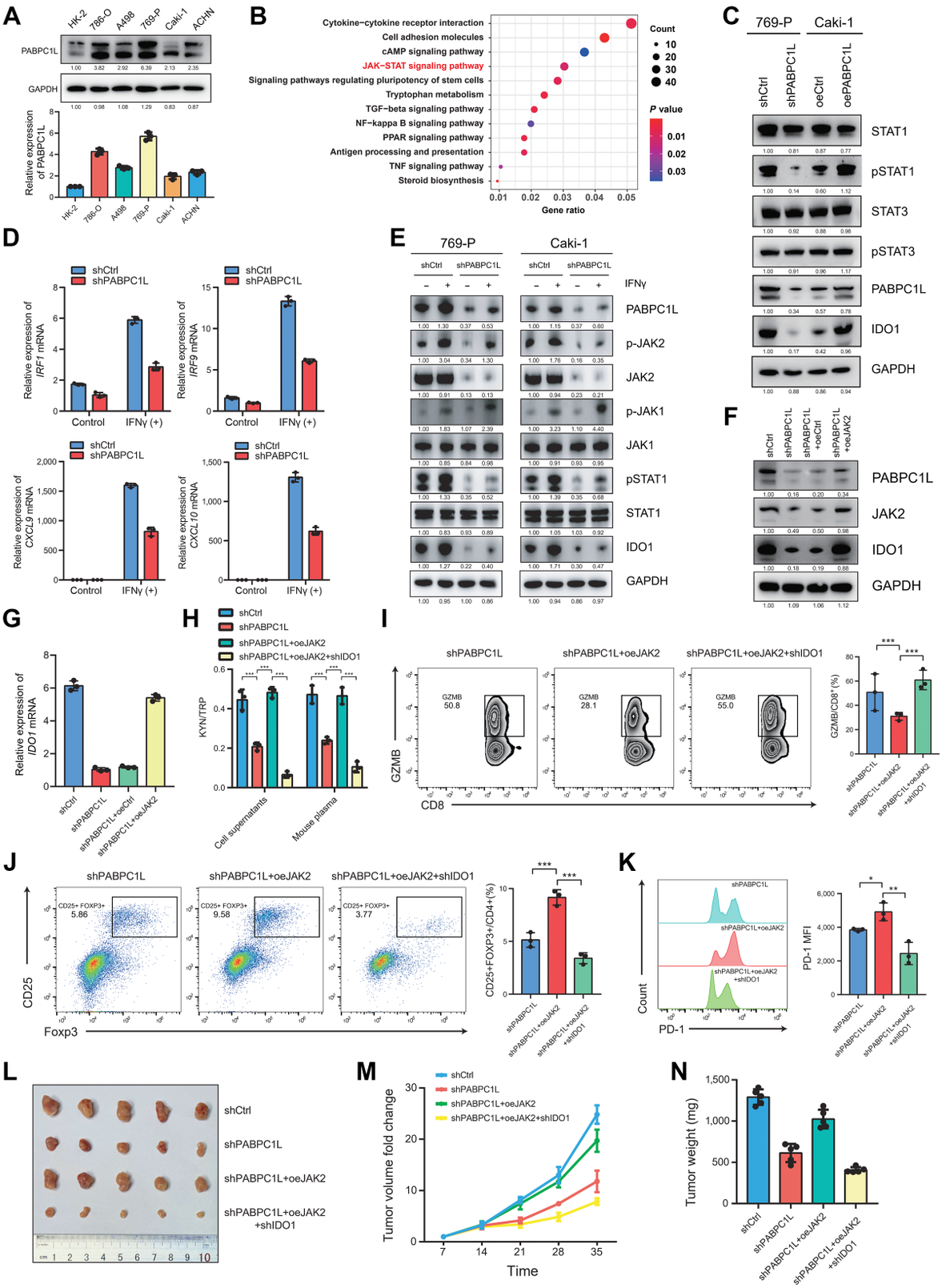
A
HK-2
786-O
A498
769-P
Caki-1
ACHN
PABPC1L
GAPDH
Relative expression of PABPC1L
B
Cytokine−cytokine receptor interaction
Cell adhesion molecules
cAMP signaling pathway
JAK−STAT signaling pathway
Signaling pathways regulating pluripotency of stem cells
Tryptophan metabolism
TGF−beta signaling pathway
NF−kappa B signaling pathway
PPAR signaling pathway
Antigen processing and presentation
TNF signaling pathway
Steroid biosynthesis
Count
P value
Gene ratio
C
769-P
Caki-1
shCtrl
shPABPC1L
oeCtrl
oePABPC1L
STAT1
pSTAT1
STAT3
pSTAT3
PABPC1L
IDO1
GAPDH
D
shCtrl
shPABPC1L
Relative expression of IRF1 mRNA
Relative expression of IRF9 mRNA
Relative expression of CXCL9 mRNA
Relative expression of CXCL10 mRNA
Control
IFNγ (+)
E
769-P
Caki-1
IFNγ
PABPC1L
p-JAK2
JAK2
p-JAK1
JAK1
pSTAT1
STAT1
IDO1
GAPDH
F
shCtrl
shPABPC1L +oeCtrl
shPABPC1L +oeJAK2
PABPC1L
JAK2
IDO1
GAPDH
G
Relative expression of IDO1 mRNA
shCtrl
shPABPC1L
shPABPC1L+oeCtrl
shPABPC1L+oeJAK2
H
shCtrl
shPABPC1L
shPABPC1L+oeJAK2
shPABPC1L+oeJAK2+shIDO1
KYN/TRP
Cell supernatants
Mouse plasma
I
shPABPC1L
shPABPC1L+oeJAK2
shPABPC1L+oeJAK2+shIDO1
GZMB
CD8
GZMB 50.8
GZMB 28.1
GZMB 55.0
GZMB/CD8+ (%)
J
shPABPC1L
shPABPC1L+oeJAK2
shPABPC1L+oeJAK2+shIDO1
CD25+ FOXP3+ 5.86
CD25+ FOXP3+ 9.58
CD25+ FOXP3+ 3.77
CD25
Foxp3
CD25+FOXP3+/CD4+(%)
K
shPABPC1L
shPABPC1L+oeJAK2
shPABPC1L+oeJAK2 +shIDO1
Count
PD-1
PD-1 MFI
L
shCtrl
shPABPC1L
shPABPC1L+oeJAK2
shPABPC1L+oeJAK2 +shIDO1
M
shCtrl
shPABPC1L
shPABPC1L+oeJAK2
shPABPC1L+oeJAK2+shIDO1
Tumor volume fold change
Time
N
Tumor weight (mg)
shCtrl
shPABPC1L
shPABPC1L+oeJAK2
shPABPC1L+oeJAK2 +shIDO1

percentages of $CD8^+$ T cells within 30–60, 60–90, 90–120, and 120–150 μm intervals were noticeably elevated in comparison with low *PABPC1L*-expressing samples (**Fig. 3E** and **F**; Supplementary Fig. S3C). To gain deeper insights into the impact of *PABPC1L* expression in tumor cells on $CD8^+$ tumor-infiltrating lymphocytes, we extracted and reclustered the $CD8^+$ T cells from the aforementioned single-cell sample data. Cell clustering analysis revealed eight subpopulations of $CD8^+$ T cells as illustrated in a UMAP plot (Supplementary Fig. S3D). Expression of canonical T-cell markers confirmed the successful classification of $CD8^+$ T cells (Supplementary Fig. S3E). Cluster 3 specifically expressed naïve markers like *Lef1* and *Ccr7* was composed of naïve T cells. Cluster 2 was characterized by elevated expression of genes associated with T-cell exhaustion, representing exhausted $CD8^+$ T cells (T_{ex}). Cluster 1 exhibited high expression levels of cytotoxic effectors and low levels of exhaustion-related genes, and was referred to as effector T cells (T_{eff}). Cluster 5 was composed of proliferating T cells according to maker genes (Supplementary Fig. S3F). Subsequently, we compared the abundance of each subpopulation in *PABPC1L*-high samples and *PABPC1L*-low samples. We observed an increase in the $CD8^+$ T_{eff} subpopulation (Cluster 1) in *PABPC1L*-low tumors, while the $CD8^+$ T_{ex} subpopulation (Cluster 2) decreased (**Fig. 3G**; Supplementary Fig. S3G). The expression levels of cytotoxicity and exhaustion genes further substantiated the enhanced effector function and reduced dysfunction of $CD8^+$ T cells in *PABPC1L*-low samples (Supplementary Fig. S3H). To elucidate paths of cell-state transitions within the clusters of $CD8^+$ T cells, we employed the Monocle3 algorithm to construct potential developmental trajectories of cluster 1, cluster 2, cluster 3, and cluster 5. Intriguingly, predominant evolutionary branches were discerned, with cluster 1 and 2 situated at the termini of distinct branches (**Fig. 3H**). This analysis demonstrated distinct differentiation trajectories of $CD8^+$ T cells in the TME modulated by *PABPC1L*. $CD8^+$ T cells infiltrating *PABPC1L* low-expressing tumors exhibited a predilection for differentiation into effector T cells rather than exhausted T cells. Collectively, these findings imply that *PABPC1L* expression in tumors is associated with elevated infiltration of Tregs, suppressed cytotoxicity of $CD8^+$ T cells, and directing T-cell differentiation toward dysfunctional trajectories.

PABPC1L regulates Tregs infiltration through JAK-STAT-IDO1 pathway in RCC

Subsequently, we explored the biological mechanism underlying *PABPC1L*-mediated upregulation of Tregs infiltration and immune response suppression. To select the suitable RCC cell lines, *PABPC1L* expression was quantified in a panel of RCC cell lines, including 786-O, ACHN, 769-P, Caki-1, and A498, as well as an immortalized renal epithelial cell line, HK-2. Western blotting and qPCR analyses revealed significant upregulation of PABPC1L protein and mRNA levels, respectively, in all RCC cell lines in comparison with the primary normal HK-2 cells (**Fig. 4A**; Supplementary Fig. S4A). In addition, a previous study indicated that the protein-coding splice variant of *PABPC1L* is predominantly expressed in human oocytes, while a noncoding splice variant subjected to nonsense-mediated decay is the major splice variant expressed in somatic tissues (31). Nonetheless, our Western blotting assays revealed abundant PABPC1L protein in RCC cell lines. Consequently, we performed a heminested PCR analysis, demonstrating that HK-2 cells primarily expressed the noncoding splice variant of *PABPC1L*, whereas RCC cells predominantly expressed the full-length coding splice variant of *PABPC1L* (Supplementary Fig. S4B). On the basis of endogenous *PABPC1L* levels, we elected to knock down *PABPC1L* in 769-P and 786-O cells and overexpress it in Caki-1 cells. RNA-seq of 769-P cells revealed substantial transcriptional alterations upon *PABPC1L* knockdown, containing 1,789 upregulated and 1,215 downregulated transcripts with $|\log_2(\text{fold change})| > 1$, and P-value <0.05 (Supplementary Fig. S4C; Supplementary Data S1). *IDO1*, previously reported to enhance intratumoral accumulation of immunosuppressive Tregs, emerged as the top dysregulated candidate following *PABPC1L* knockdown. The association between *IDO1* and *PABPC1L* is further revealed by our examination of published RCC scRNA-seq data. Indeed, the IDO1-high RCC cell population largely overlaped with cells exhibiting elevated expression of *PABPC1L* (Supplementary Fig. S4D). Gene Ontology and Kyoto Encyclopedia of Genes and Genomes (KEGG) analysis (**Fig. 4B**; Supplementary Fig. S4E) also demonstrated that DEGs were functionally enriched in pathways related to immune function. Notably, the JAK/STAT pathway has been implicated in immunotherapy responsiveness in numerous studies (32, 33). The RNA-seq findings were further corroborated by Western blotting analysis. *PABPC1L* knockdown substantially decreased the protein levels of pSTAT1, while *PABPC1L* overexpression produced the opposite effect (**Fig. 4C**). Consequently, our results suggest that *PABPC1L* enhances JAK/STAT1 signaling pathway activity in RCC cells. IFNγ stimulation is known to activate the JAK/STAT1 signaling pathway and consequently upregulate *IDO1* (34). In line with this, IFNγ stimulation resulted in increased expression of *IDO1* and *STAT1* target genes in 769-P and Caki-1 cells (**Fig. 4D**; Supplementary Fig. S4F). Moreover, *PABPC1L* depletion led to a noticeable reduction in the overall protein abundance of JAK2 and the expression of JAK/STAT1 target genes induced by IFNγ. It also suppressed the phosphorylation of JAK2 and STAT1, which were induced by IFNγ, along with the upregulation of IDO1 protein level (**Fig. 4D** and **E**; Supplementary Fig. S4G). The total level and phosphorylation level of

Figure 4.

Loss of *PABPC1L* impairs JAK-STAT-IDO1 pathway in RCC. **A,** Representative Western blot (top) and statistical analysis (bottom) in the immortalized HK-2 renal epithelial cell line and RCC cell lines. GAPDH was used as a loading control. **B,** KEGG analysis showed the significantly altered signaling pathways after *PABPC1L* silencing in RCC cells. **C,** Representative Western blot analysis of STAT1, STAT3, pSTAT1, and pSTAT3 protein expression levels in 769-P cells with *PABPC1L* knockdown (left) and in Caki-1 cells with *PABPC1L* overexpression (right). **D,** mRNA expression of JAK-STAT1 target genes in shCtrl and shPABPC1L 769-P cells with or without IFNγ stimulation. Cells were treated with 100 U/mL IFNγ. **E,** Representative Western blot analysis showing JAK1, p-JAK1, JAK2, p-JAK2, STAT1, pSTAT1, and IDO1 protein expression levels in 769-P (left) and Caki-1 (right) cells with *PABPC1L* knockdown. Cells were stimulated with or without 100 U/mL IFNγ. **F,** Effects of JAK2 overexpression on IDO1 protein expression in shCtrl and shPABPC1L 769-P cells. **G,** Effects of JAK2 overexpression on *IDO1* mRNA expression in shCtrl and shPABPC1L 769-P cells. **A–G,** All experiments were performed with three independent biological replicates, and data shown are representative of three independent experiments. **H,** Differently treated cells were cultured for 24 hours without KYNU treatment. KYN and TRP levels in cell supernatants were determined by ELISA. Differently treated cells were injected subcutaneously into BALB/c mice. HPLC/MS-MS analysis was used to generate the TRP metabolomic profiles of mouse plasma, and the KYN/TRP ratio in the mouse plasma was calculated. **I,** Flow cytometry analysis of GZMB+ in $CD8^+$ T cells. **J,** Flow cytometry analysis of $CD25^+$ and $Foxp3^+$ Tregs in $CD4^+$ T cells. **K,** Representative flow cytometry histograms and statistical analysis of cell surface PD-1 with the indicated treatments. **L** and **M,** Representative images of tumors (**L**) and growth curves (**M**) of indicated Renca tumors in BALB/c mice ($n = 5$ per group). **N,** Tumor weight measured after surgical dissection ($n = 5$ per group). *, $P < 0.05$; **, $P < 0.01$; ***, $P < 0.001$.

JAK1, another upstream kinase of STAT1, remained unaffected by *PABPC1L* knockdown. To determine whether IDO1 downregulation resulted from decreased JAK2 levels in *PABPC1L* knockdown cells, a rescue experiment involving *JAK2* overexpression was conducted. *JAK2* overexpression successfully restored *IDO1* expression in *PABPC1L* knockdown cells (**Fig. 4F** and **G**). In summary, these findings confirm the role of *PABPC1L* in enhancing JAK2-STAT1 signaling activity, thereby promoting *IDO1* expression.

According to prior research, *IDO1* encodes for indoleamine 2,3-dioxygenase, which is an enzyme responsible for the primary and rate-determining step of TRP catabolism, leading to N-formylkynurenine (KYN). And a depletion of TRP can hinder the division of T lymphocytes, while an accumulation of TRP catabolites can induce T-cell apoptosis and promote the differentiation of Tregs (9, 10). Furthermore, considering our findings that *IDO1* is modulated by PABPC1L via the JAK2-STAT1 signaling axis, we hypothesize that PABPC1L regulates Treg infiltration and the resultant immunosuppressive TME, a process instigated by TRP degradation and KYN accumulation. Therefore, targeting PABPC1L might be a plausible strategy to effectively counteract this immunosuppression.

To investigate this hypothesis, we knocked down *PABPC1L* or simultaneously knocked down *PABPC1L* and overexpressed *JAK2* in the Renca cell line. We observed that *PABPC1L* knockdown substantially reduced the KYN/TRP ratio, whereas concurrent *PABPC1L* knockdown and *JAK2* overexpression elevated the KYN/TRP ratio in cell supernatants *in vitro* and in the plasma of a subcutaneous mouse model, as determined by ELISA or HPLC/MS-MS analyses. The increased KYN/TRP ratio observed upon *PABPC1L* knockdown and *JAK2* overexpression was reversed by *IDO1* knockdown (**Fig. 4H**). Flow cytometry analyses were conducted to assess T-cell infiltration within tumors. The results revealed that *PABPC1L* knockdown substantially increased the proportion of GZMB+ cells within the $CD8^+$ T-cell population, while concurrently reducing the proportions of $CD25^+FOXP3^+$ cells among $CD4^+$ T cells and PD-1+ cells among $CD8^+$ T cells in the tumors. *PABPC1L* knockdown in conjunction with *JAK2* overexpression reversed the aforementioned effects; however, *IDO1* knockdown restored the elevated proportion of GZMB+ cells among $CD8^+$ T cells, diminished the proportion of $CD25^+FOXP3^+$ cells among $CD4^+$ T cells, and decreased the proportion of PD-1+ cells among $CD8^+$ T cells (**Fig. 4I–K**). Further we performed extra *in vivo* subcutaneous tumor formation experiments and recorded subcutaneous tumor growth curves. We found that *IDO1* knockdown could restore the tumor growth rate upon *PABPC1L* knockdown and *JAK2* overexpression (**Fig. 4L–N**). In summary, these data indicate that *PABPC1L* contributes to Tregs infiltration and immune suppression by modulating *IDO1* expression via a *JAK2*-associated pathway in tumor cells.

PABPC1L directly regulates JAK2 expression by promoting *JAK2* mRNA stability and translation

The *PABPC1L* gene belongs to the poly(A)-binding protein (PABP) family, which has been demonstrated to interact with the 5′ untranslated region of mRNA transcripts. This interaction can promote translation initiation by facilitating the recruitment of the translation initiation complex (20). Furthermore, PABPC1L can also bind to the poly(A) tail of mRNA, playing a role in protecting mRNA from degradation by nucleases (35). To further elucidate the molecular mechanisms of PABPC1L function in *IDO1* regulation, we conducted RNA immunoprecipitation and RIP sequencing (RIP-seq) with an anti-PABPC1L antibody. RIP-seq indicated that PABPC1L bound to numerous mRNAs, including *JAK2* mRNA, but not *IDO1* mRNA (Supplementary Data S2). Subsequent qPCR amplification of the immunoprecipitated RNAs revealed that PABPC1L bound to *JAK2* mRNA but not *IDO1* mRNA (**Fig. 5A**; Supplementary Fig. S4H). Consequently, we postulate that PABPC1L exerts its activity by protecting and promoting *JAK2* mRNA translation. This hypothesis was substantiated through the subsequent experiments. First, RNA-FISH assays demonstrated the colocalization of *JAK2* mRNA and PABPC1L in the cytoplasm (**Fig. 5B**). Second, Flag-tagged PABPC1L was stably overexpressed in 769-P and Caki-1 cells, followed by a pulldown assay, revealing PABPC1L's association with translation initiation factor eIF4G (**Fig. 5C**). Notably, JAK2 and IDO1 were not detected as immunoprecipitants with the anti-PABPC1L antibody according to MS results (Supplementary Data S3). Reciprocally, the endogenous interaction between PABPC1L and eIF4G was corroborated in 769-P and Caki-1 cells via a coimmunoprecipitation assay (**Fig. 5D**). To further validate the association of PABPC1L with the eIF4F complex, we conducted an m^7GTP cap pulldown assay in cells with *PABPC1L* knockdown or overexpression. Subsequent immunoblot analysis of proteins interacting with the m^7G cap revealed that the absence of PABPC1L diminished the binding of eIF4E and eIF4G to the m7G cap analog. Conversely, overexpression of PABPC1L exhibited the opposite effect (**Fig. 5E**). Third, *PABPC1L* downregulation significantly impeded *JAK2* mRNA stability in the 769-P cell line following actinomycin D treatment, a transcription inhibitor (**Fig. 5F**). Conversely, *PABPC1L* overexpression enhanced *JAK2* mRNA stability in the Caki-1 cell line (Supplementary Fig. S4I). In accordance with previous studies (36) that reported RRM1–2 as the principal binding domains within the poly(A) binding protein family, our RIP assays employing individual RNA recognition motif (RRM) domain truncations verified that both RRM1 and RRM2 were responsible for PABPC1L and *JAK2* mRNA binding (**Fig. 5G**). Fourth, we performed polysome fractionation analyses to determine whether PABPC1L influences the translation efficiency of all or specific mRNAs. Our findings indicated that *PABPC1L* depletion did not impact global polyribosome formation (**Fig. 5H**). Furthermore, we conducted RT-qPCR on each polysome fraction in control and *PABPC1L*-depleted cells, revealing a leftward shift in the distribution of *JAK2* mRNAs on the fractionation gradient (**Fig. 5I**). This observation suggests that *JAK2* mRNAs were associated with smaller polysomes upon *PABPC1L* depletion, implying a suppression of *JAK2* mRNA translation efficiency in *PABPC1L*-depleted cells. In summary, these findings confirm that PABPC1L exerts its activity by protecting and promoting *JAK2* mRNA translation. In this study, we identify *PABPC1L* as a crucial regulator of the JAK2/STAT1/IDO1 signaling pathway.

JAK2-STAT1 signaling contributes to *PABPC1L* upregulation in RCC through a positive feedback loop

Because *PABPC1L* is upregulated in RCC, we investigated the mechanism contributing to *PABPC1L* overexpression. Because we observed a slight increased expression of PABPC1L protein upon IFNγ stimulation and the *JAK2* overexpression rescue experiment in RCC cells (**Fig. 4E** and **F**), we analyzed the promoter sequence of *PABPC1L* by JASPAR and surprisingly identified two STAT binding sites that could be bound by STAT1 within −677 to −667 bp and −643 to −633 bp upstream of the *PABPC1L* transcription start site (**Fig. 6A**). A series of reporter plasmids, containing sequential deletion of the 5′ flanking sequence upstream of *PABPC1L* promoter, was transfected into 769-P cells. A luciferase reporter assay indicated that sequence deletions from −2,000 to −650 bp upstream of the transcription start site of *PABPC1L* did not influence the promoter activity but that

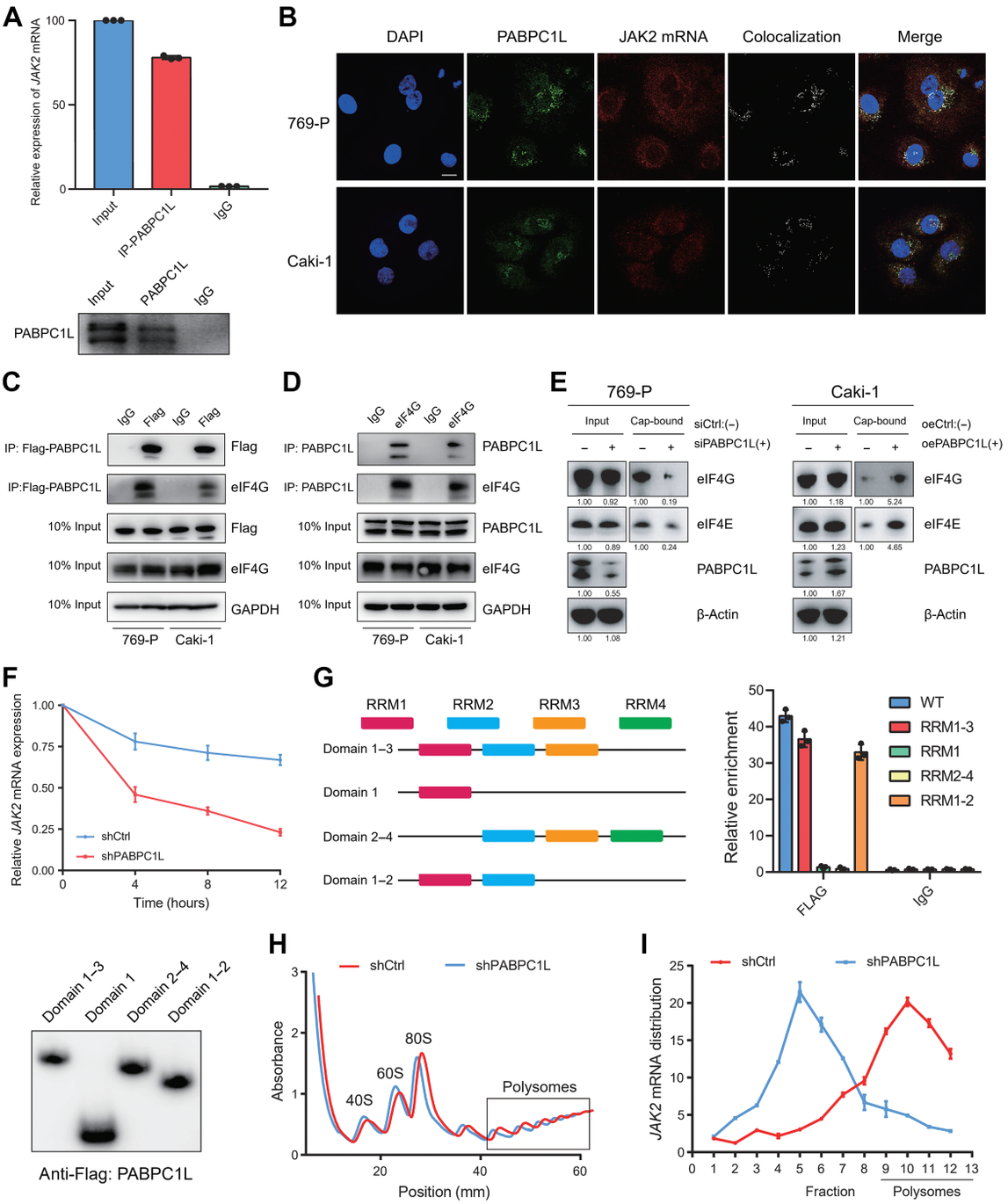

Figure 5.

Binding of PABPC1L to *JAK2* mRNA promotes its stability and translation. **A,** RIP assays showed the association of PABPC1L with *JAK2* mRNA. Relative enrichment representing RNA levels associated with PABPC1L compared with input control. IgG antibody served as a control. **B,** IF-FISH assay showing that *JAK2* mRNA is colocalized with PABPC1L protein in the cytoplasm. Scale bar, 10 μm. **C,** Representative Western blot analysis showing the coimmunoprecipitation of overexpressed PABPC1L-Flag and endogenous eIF4G in both 769-P and Caki-1 cells. **D,** Representative Western blot analysis showing the coimmunoprecipitation of endogenous PABPC1L and eIF4G in both 769-P and Caki-1 cells. **E,** PABPC1L expression was altered and cell lysates were incubated with m^7GTP (5′mRNA cap analog). Cap-associated proteins were then eluted and immunoblotted using the antibodies indicated. **F,** Reduced stability of *JAK2* mRNA upon *PABPC1L* knockdown. **G,** Left, schematic representation of PABPC1L and its truncated forms. Sequence and structure analyses indicate the presence of RRM1–4. Right, relative enrichment represented *JAK2* mRNA levels associated with truncated PABPC1L relative to input control. Bottom, immunoblot analysis with anti-FLAG of cells transfected with plasmids encoding FLAG-tagged truncated PABPC1Ls. **H,** Representative traces of polyribosome profiles obtained from shCtrl or shPABPC1L cells. **I,** qRT-PCR analysis of *JAK2* mRNA levels in each fraction obtained from shCtrl or shPABPC1L cells. All experiments were performed with three independent biological replicates, and data shown are representative of three independent experiments.

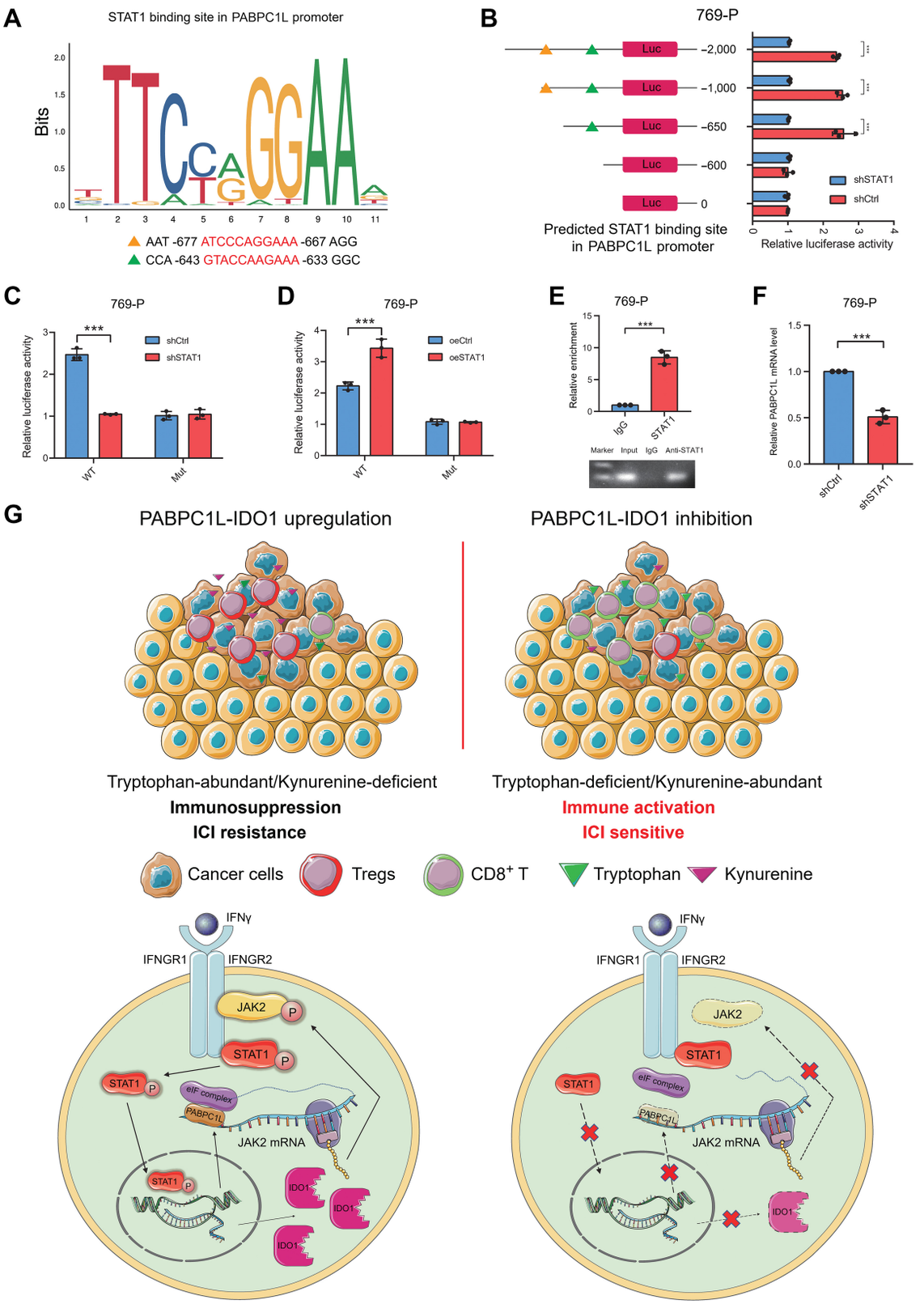
A
STAT1 binding site in PABPC1L promoter
Bits
AAT -677 ATCCCAGGAAA -667 AGG
CCA -643 GTACCAAGAAA -633 GGC
B
769-P
Luc
-2,000
-1,000
-650
-600
0
shSTAT1
shCtrl
Predicted STAT1 binding site in PABPC1L promoter
Relative luciferase activity
C
769-P
Relative luciferase activity
shCtrl
shSTAT1
WT
Mut
D
769-P
Relative luciferase activity
oeCtrl
oeSTAT1
WT
Mut
E
769-P
Relative enrichment
IgG
STAT1
Marker
Input
IgG
Anti-STAT1
F
769-P
Relative PABPC1L mRNA level
shCtrl
shSTAT1
G
PABPC1L-IDO1 upregulation
PABPC1L-IDO1 inhibition
Tryptophan-abundant/Kynurenine-deficient
Immunosuppression
ICI resistance
Tryptophan-deficient/Kynurenine-abundant
Immune activation
ICI sensitive
Cancer cells
Tregs
CD8+ T
Tryptophan
Kynurenine
IFNγ
IFNGR1
IFNGR2
JAK2
STAT1
eIF complex
PABPC1L
JAK2 mRNA
IDO1

deletion to −600 bp significantly reduced the promoter activity (**Fig. 6B**). Moreover, mutating the −643 to −633 bp STAT binding sites resulted in the abolishment of promoter activity following reporter plasmid transfection (**Fig. 6C**). Knockdown of *STAT1*, which is highly expressed in 769-P cells, markedly abolished *PABPC1L* promoter activity in 769-P cells (**Fig. 6B** and **C**). In contrast, ectopic expression of *STAT1* elevated the promoter activity of wild-type but not mutant *PABPC1L* STAT binding sites (**Fig. 6D**). Moreover, chromatin immunoprecipitation followed by qPCR assays (ChIP-qPCR) using an anti-STAT1 antibody further confirmed the STAT1-specific binding sequences in 769-P cells (**Fig. 6E**). Similar results were observed in the 786-O cell line, which is another RCC cell line (Supplementary Fig. S5A and S5B). In line with the above results, *PABPC1L* expression was downregulated in 769-P cells with *STAT1* knockdown, but it was upregulated in Caki-1 cells with *STAT1* overexpression (**Fig. 6F**; Supplementary Fig. S5C). Collectively, these data reveal that JAK2-STAT1, which elevated by *PABPC1L* expression, participates in a positive feedback loop to promote the transcription of *PABPC1L* in RCC (**Fig. 6G**).

Inhibition of *PABPC1L* expression overcomes immunosuppression in an IDO1-dependent manner and enhances ICB responsiveness in PDX models

The JAK-STAT signaling pathway is known for its complexity and multifunctional roles in immune regulation. To elucidate whether additional functions of JAK2-STAT1 in immune modulation and cell apoptosis might contribute to the tumorigenic processes associated with *PABPC1L*, we engineered *IDO1* knockout cell lines alongside respective control lines. IDO1-deficient cells (IDO1-KO) were generated using CRISPR-CAS9 technique. These cells were subjected to both knockdown and overexpression of *PABPC1L* to examine the resultant phenotypic alterations in both *in vivo* and *in vitro* settings. Our observations revealed a marked decrease in various phenotypic manifestations, including the KYN/TRP ratio, Tregs infiltration, and tumor growth in *IDO1* knockout cells relative to the controls (**Fig. 7A–D**). This finding confirms that *PABPC1L* regulates TRP metabolism and immunosuppression in an IDO1-dependent manner.

Because IDO1 is an important innate immune regulator that acts by triggering TRP metabolism in the TME, targeting IDO1 was once thought to be promising approach for cancer immunotherapy, extending beyond ICB. However, recent clinical trials involving IDO1 inhibitors have encountered significant challenges, with the underlying causes including potential off-target effects and alternative activation of the mTOR pathway. In light of the above, we further sought to investigate the potential of targeting *PABPC1L* in human tumors to enhance the therapeutic efficacy of cancer immunotherapy instead of directly targeting IDO1. To more accurately mimic the RCC TME, we employed a preclinical model, in which immunocompromised NCG mice were implanted with RCC PDXs and subsequently subjected to tumor-specific $CD8^+$ T cells and Tregs transfer (28, 37). A specific siRNA targeting *PABPC1L* was utilized to examine the impact of *PABPC1L* inhibition on anti-PD-1 therapy in a humanized immune system model (**Fig. 7E**). Treatment with siRNA effectively abrogated *PABPC1L* expression in PDX tumor tissues (Supplementary Fig. S5D). In alignment with previous findings, *PABPC1L* siRNA exerted negligible effects on PDX tumor growth in NCG mice without immune reconstitution (Supplementary Fig. S5E). Further analysis revealed that although both *PABPC1L* siRNA and anti-PD-1 monotherapy suppressed tumor growth and extended OS, the combination of siPABPC1L and PD-1 blockade exhibited a remarkable reduction in tumor burden and enhanced OS compared with treatment with siPABPC1L or anti-PD-1 antibody alone (**Fig. 7F–H**). In addition, flow cytometry analyses demonstrated that siPABPC1L or anti-PD-1 monotherapy slightly, while the combination of siPABPC1L and anti-PD-1 substantially, increased the proportion of GZMB+ cells among $CD8^+$ T cells and reduced the proportion of PD-1+ cells among $CD8^+$ T cells in the tumors (**Fig. 7I** and **J**). Moreover, the number of cleaved caspase-3–positive tumor cells exhibited a substantial increase in the combination treatment group, suggesting that the concurrent administration of siPABPC1L and anti-PD-1 constitutes a highly effective therapeutic strategy for RCC (**Fig. 7K**). Collectively, these findings provide convincing evidence that *PABPC1L* inhibition enhances the therapeutic effects of PD-1 blockade and may represent a promising target for improving cancer immunotherapy efficacy in RCC.

Discussion

Tumor-infiltrating lymphocytes have been extensively reported to confer survival advantages in various tumor types, including lung, colon, and breast cancers (38–40). $CD8^+$ cytotoxic T cells constitute a vital component of cancer immune surveillance. An increased infiltration of $CD8^+$ T cells within TME is correlated with favorable prognostic indicators and can potentially predict the response to ICB in specific cancer types (5, 41, 42). However, in certain cancer types, particularly RCCs, elevated $CD8^+$ T-cell infiltration levels fail to exhibit a correlation with survival benefits (43).

Intriguingly, a recent proteogenomic analysis of RCC revealed that the GP1 subtype, with the most robust immune features, correlated with the poorest clinical outcomes (8). A previous study indicated that RCC utilizes T-cell dysfunction strategy, which impairs the ability of cytotoxic T cells to kill tumor cells, rather than T-cell exclusion strategy (44). Tregs, crucial for immune self-tolerance, secrete cytokines or directly inhibit effector T cells, suppressing antitumor immunity in the TME. Increased Treg infiltration significantly reduces immune checkpoint inhibitors' efficacy (45, 46). Nonetheless, the molecular mechanisms underlying immune suppression and immune escape within the RCC microenvironment warrant further elucidation. In our previous study, we identified *PABPC1L* as a hypoxia-immune biomarker for RCC (23). In the current study, we identified *PABPC1L* as a pivotal contributor to tumor immune evasion in RCC.

Figure 6.
PABPC1L is a transcriptional target of STAT1. **A,** Conserved STAT binding sites at the *PABPC1L* promoter were predicted by JASPAR. **B,** Luciferase reporter assays for 769-P cells with or without STAT1 silencing transfected with indicated reporter plasmids containing full length and truncated *PABPC1L* promoters. **C,** Luciferase reporter assays for 769-P cells with or without STAT1 silencing transfected with indicated reporter plasmids containing wild-type (WT) and mutant (Mut) *PABPC1L* promoters. **D,** Luciferase reporter assays indicated that STAT1 enhanced wild-type but not mutant *PABPC1L* promoter activity. **E,** ChIP assays showed that STAT1 bound to the *PABPC1L* promoter in 769-P cells (top). The ChIP products were analyzed by electrophoresis (bottom). **F,** Relative RNA expression level of *PABPC1L* by qPCR in 769-P cells with STAT1 silencing. **G,** Top, schematic representations of the role of the PABPC1L/IDO1 axis in immune suppression and ICB resistance in RCC. Bottom, schematic model depicting the molecular mechanism of *PABPC1L* regulating IDO1 expression and JAK2-STAT1 signaling contributing to PABPC1L upregulation in RCC through a positive feedback loop. All experiments were performed with three independent biological replicates, and data shown are representative of three independent experiments. ***, $P < 0.001$.

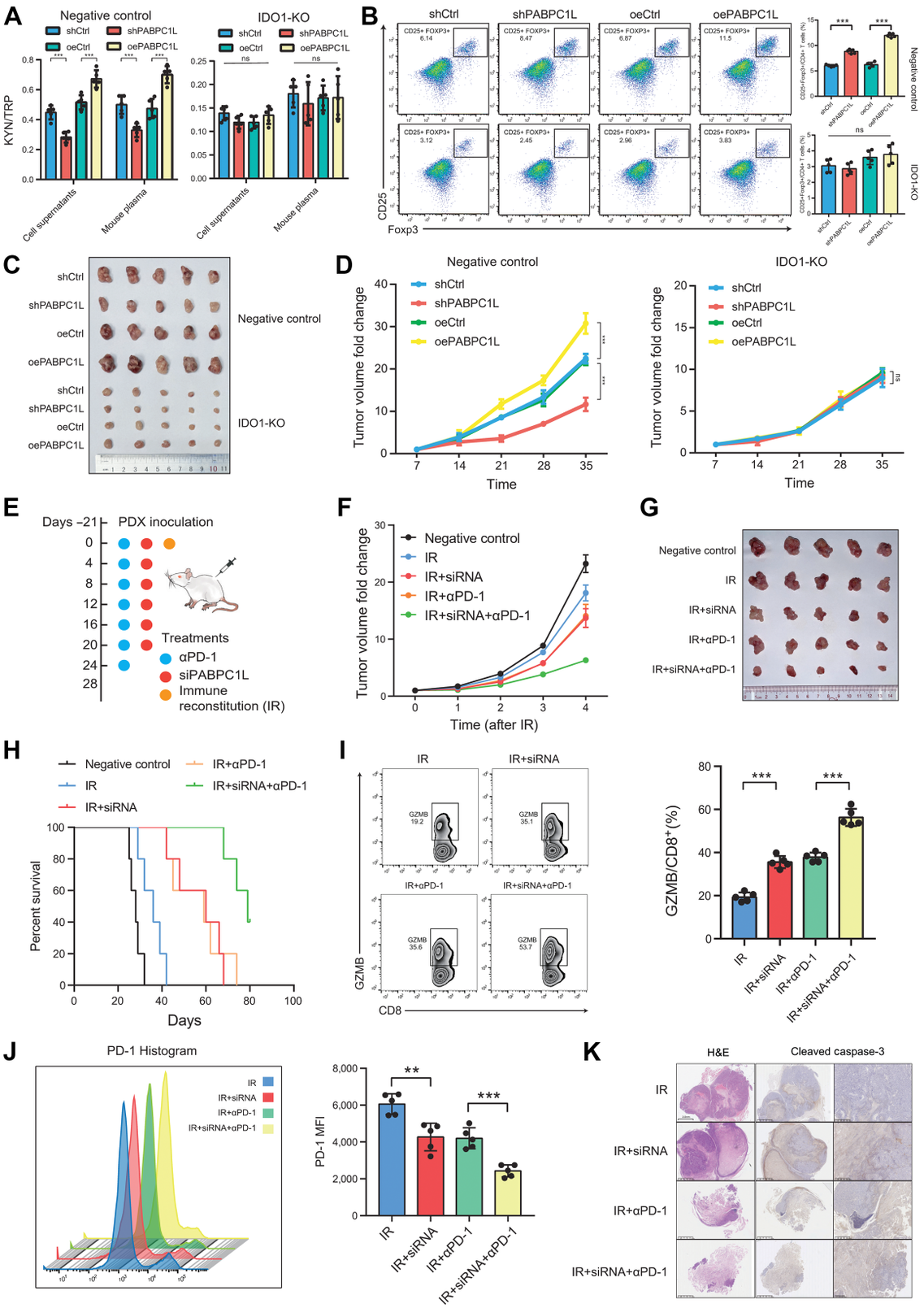
A
Negative control
IDO1-KO
shCtrl
shPABPC1L
oeCtrl
oePABPC1L
KYN/TRP
Cell supernatants
Mouse plasma
ns
B
shCtrl
shPABPC1L
oeCtrl
oePABPC1L
CD25+ FOXP3+
CD25
Foxp3
Negative control
IDO1-KO
C
shCtrl
shPABPC1L
oeCtrl
oePABPC1L
Negative control
IDO1-KO
D
Negative control
IDO1-KO
Tumor volume fold change
Time
E
Days −21
PDX inoculation
0
4
8
12
16
20
24
28
Treatments
αPD-1
siPABPC1L
Immune reconstitution (IR)
F
Negative control
IR
IR+siRNA
IR+αPD-1
IR+siRNA+αPD-1
Tumor volume fold change
Time (after IR)
G
Negative control
IR
IR+siRNA
IR+αPD-1
IR+siRNA+αPD-1
H
Negative control
IR
IR+siRNA
IR+αPD-1
IR+siRNA+αPD-1
Percent survival
Days
I
IR
IR+siRNA
IR+αPD-1
IR+siRNA+αPD-1
GZMB
CD8
GZMB/CD8+(%)
J
PD-1 Histogram
IR
IR+siRNA
IR+αPD-1
IR+siRNA+αPD-1
PD-1 MFI
K
H&E
Cleaved caspase-3
IR
IR+siRNA
IR+αPD-1
IR+siRNA+αPD-1

PABPC1L gene at 20q13 encodes a protein influencing mRNA. Initially linked with oocyte and embryo development (31), recent research shows its significant role in cancer, especially as a prognostic marker in colorectal (21) and prostate cancer (22). Our findings identify *PABPC1L* as a biomarker of hypoxic-immunosuppressive state in RCC (23). The current study found elevated *PABPC1L* expression in RCC at protein and mRNA levels, linked to immune dysfunction and poor prognosis (TCGA-KIRC, Checkmate cohorts, and our RCC patient cohort). Using immunocompetent and immunodeficient mouse models, *PABPC1L* depletion inhibited tumor growth and prolonged survival, enhancing antitumor immunity. Single-cell sequencing datasets revealed high *PABPC1L* expression in RCC induces Tregs infiltration and reduces $CD8^+$ T-cell presence, promoting TME dysfunction. T cells cocultured with *PABPC1L*-deficient kidney tumor cells showed increased antitumor activity, highlighting *PABPC1L*'s immunosuppressive role in RCC.

IDO1 exhibits frequent overexpression in both neoplastic and stromal cells within the TME (47), serving as a pivotal enzyme that orchestrates TRP catabolism, ultimately resulting in KYN accumulation (9). Through activation of the AhR signaling cascade, IDO1 modulates *FOXP3* expression in $CD4^+$ T lymphocytes, subsequently augmenting the Treg population (16). Moreover, IDO1 elevates the expression of PD-1 in $CD8^+$ T cells, impairing the proliferation of these cells (16). The expression of *IDO1* is significantly upregulated at the transcriptional level in response to inflammatory agents, including IFNs, TNFα, as well as pathogen-associated and damage-associated molecular patterns (PAMP and DAMP, respectively; ref. 11). Concurrently, oncogenic signaling cascades, such as KIT, RAS, JAK-STAT, and NFκB pathways, contribute to the upregulation of IDO1 mRNA expression (48–50). Despite these observations, the molecular mechanism prompting *IDO1* overexpression in RCC cells warrant further investigation. In the current study, we validate IFNγ stimulates tumor cells to overexpress *IDO1* through the JAK-STAT pathway. IFNγ binds to interferon receptor and transactivates JAKs (JAK1and JAK2), thereby activating the JAK-STAT signaling pathway (mainly through STAT1). Phosphorylated STAT1 interacts with the *IDO1* promoter region, thereby stimulating *IDO1* transcription in RCC. Consistently, we found that *PABPC1L* upregulated JAK2-STAT1 signaling to promote *IDO1* expression. Intriguingly, PABPC1L was identified to complex with the translation initiation factor eIF4G, consequently promoting *JAK2* mRNA translation and acting as a pivotal modulator of the JAK2/STAT1/IDO1 signaling axis. Moreover, JAK2-STAT1 upregulation, mediated by *PABPC1L* expression, participates in a positive feedback loop that enhances *PABPC1L* transcription in RCC. An elevation in PABPC1L protein expression was observed following IFNγ stimulation and *JAK2* overexpression. Phosphorylated STAT1 interacts with the *PABPC1L* promoter, leading to the transcriptional activation of PABPC1L in RCC. Taken together, these findings elucidated a potential molecular mechanism of JAK2/STAT1 signaling overactivation and immunosuppressive TME in RCC.

There remains a persistent unmet clinical demand for immunotherapeutic interventions in the majority of patients with RCC who exhibit resistance to ICB. IDO1 is an important innate immune regulator that acts by triggering TRP metabolism in the TME. Consequently, targeting IDO1 may be promising approach for cancer immunotherapy, extending beyond ICB. However, recent clinical trials involving IDO1 inhibitors have encountered significant challenges, with the underlying causes for these unfavorable outcomes remaining undefined. Recent studies indicated that TRP-related IDO1 inhibitors might have potential off-target effects. This phenomenon primarily arises due to the capacity of these compounds, including 1-methyl-tryptophan (1-MT), epacadostat, navoximod, and norharmane, to robustly AhR-mediated signaling. This activation subsequently leads to immunosuppression and an upregulation of IDO1 expression (51). Nevertheless, AhR activation is not the only factor that is believed to underlie the failure of IDO1 inhibitors in cancer treatment. TRP-related IDO inhibitors, which function as pseudonutritional signals by mimicking TRP, have been found to stimulate mTOR signaling in somatic cells (52). In the current study, a significant correlation was observed between low *PABPC1L* expression and enhanced benefits from $CD8^+$ T-cell infiltration in the TCGA-KIRC patient cohort. A subsequent assessment of the Checkmate cohort, which included individuals undergoing ICB treatment, revealed increased ICB therapy sensitivity in patients exhibiting reduced *PABPC1L* expression. Moreover, employing a preclinical PDX model with immune reconstitution enabled the validation of a synergistic impact resulting from the concomitant application of *PABPC1L* inhibition and ICB, as opposed to ICB monotherapy. The suppression of *PABPC1L* led to decreased IDO1 protein level and hindered IDO1-mediated TRP metabolism, simultaneously eliminating the "off-target" effects of IDO1 inhibitors on AhR activation. This process ultimately transformed the immunosuppressive TME. Notably, prior research has suggested that the protein-coding splice variant of *PABPC1L* is primarily expressed in human oocytes, whereas a noncoding splice variant subject to nonsense-mediated decay constitutes the principal splice variant in somatic tissues (31). Targeting *PABPC1L* protein-coding splice variant, which is only expressed in RCC cells rather than somatic tissues, would improve the precision of treatment and reduce side effects. In summary, the findings of this study indicate that *PABPC1L* holds significant potential as a therapeutic target for the development of innovative cancer treatments in combination with ICB.

In essence, the JAK-STAT signaling is indeed intricate, serving multifaceted roles in immune regulatory processes across various cancer types. This pathway not only mediates tumor cell recognition but also governs tumor-mediated immune evasion. High STAT1 levels are prognostically favorable in specific cancer subtypes like rectal cancer (53) and metastatic melanomas (54). However, they are also linked with immunosuppression and disease progression in RCCs (8). The contrasting outcomes of JAK/STAT inhibition in RCC versus

Figure 7.

PABPC1L deficiency reverses immune suppression and therapeutic potential of *PABPC1L* knockdown and ICB combination therapy in RCC PDX models. **A,** IDO1-KO cells and control cells were subjected to PABPC1L knockdown or overexpression. KYN and TRP levels in cell supernatants were determined by ELISA. HPLC/MS-MS analysis was used to generate the TRP metabolomic profiles of mouse plasma, and the KYN/TRP ratio in the mouse plasma was calculated. **B,** Flow cytometry analysis of $CD25^+$ and $Foxp3^+$ Tregs. **C** and **D,** IDO1-KO cells and control cells were subjected to PABPC1L knockdown or overexpression. **C,** Tumor images. **D,** Tumor growth curves ($n = 5$ per group). **E,** Schematic diagram showing that RCC PDX mice were treated with adoptive T-cell transfer, anti-PD-1 antibody, and siRNA at the indicated time points. In the figure, −21 indicates the day of subcutaneous inoculation of RCC PDXs. **F–H,** The anti-PD-1 and siPABPC1L combination therapy synergistically suppressed the growth of tumors in RCC PDX mice ($n = 5$ per group). Tumor growth curves (**F**), tumor images (**G**), and survival curves (**H**). **I,** Flow cytometry analysis of GZMB in $CD8^+$ T cells isolated from PDX tumors, with the indicated treatments. **J,** Representative flow cytometry histograms (left) and statistical analysis (right) of cell surface PD-1 isolated from PDX tumors with the indicated treatments. **K,** Representative images and quantification of cleaved caspase-3–positive cells as analyzed by IHC staining. Scale bars, 2.5 mm ($n = 5$ per group). ns, nonsignificant; ***, $P < 0.001$.

other malignancies, such as melanoma, may be traced back to inherent variances across tumor types and their respective heterogeneity. As we ponder the therapeutic prospects of targeting the PABPC1L/JAK2/STAT1/IDO1 axis in RCC, it is pivotal to exercise caution when extending this approach to other cancers where JAK/STAT signaling could be beneficial. Future investigations should aim to demystify these intricate interactions, optimizing strategies to maximize therapeutic benefits while averting potential pitfalls.

In summary, our study reveals a critical role for *PABPC1L* in facilitating immune evasion in RCC through the enhancement of *JAK2* mRNA translation. This process consequently upregulates the IFNγ/JAK2/STAT1 signaling axis and promotes the transcription of *IDO1*. Notably, the elevated JAK2-STAT1 levels, driven by *PABPC1L* expression, partake in a positive feedback loop that further stimulates *PABPC1L* transcription. The combination of *PABPC1L* inhibition and ICB, which reprograms the immunosuppressive TME and prevents immune evasion, represents a potential therapeutic strategy for improving the efficacy of cancer immunotherapy in patients with RCC.

Authors' Disclosures

No disclosures were reported.

Authors' Contributions

G. Shu: Conceptualization, data curation, formal analysis, validation, investigation. **M. Chen:** Conceptualization, software. **W. Liao:** Data curation, validation, investigation. **L. Fu:** Software, formal analysis. **M. Lin:** Formal analysis, methodology. **C. Gui:** Writing–original draft. **J. Cen:** Supervision. **J. Lu:** Visualization, methodology. **Z. Chen:** Funding acquisition. **J. Wei:** Funding acquisition. **W. Chen:** Visualization. **Y. Wang:** Writing–original draft. **J. Zhu:** Project administration. **T. Zhao:** Formal analysis. **X. Liu:** Methodology. **J. Jing:** Investigation, visualization. **G.-c. Liu:** Resources, validation. **Y. Pan:** Resources, data curation. **J. Luo:** Conceptualization, visualization, writing–review and editing. **J. Zhang:** Conceptualization, resources, funding acquisition.

Acknowledgments

This work was supported by National Natural Science Foundation of China (no. 81772514, 82073381 to J. Zhang; 81725016, 81872094 to J. Luo; 81772718 to W. Chen; 82002684 to J. Lu), Pearl River S&T Nova Program of Guangzhou (no. 201806010005 to J. Zhang), The Natural Science Foundation of Guangdong (no. S2019B151502046 to J. Zhang, 201704020174 to J. Luo, 2023A1515030038 to Z. Chen), China Postdoctoral Science Foundation (no. 236464 to J. Lu; 2023M730374 to Y. Pan; 2021TQ0381, 2021M703700 to J. Cen), Research foundation of Guangzhou Women and Children's Medical Center for Clinical Doctor (no. 2023BS017 to G. Shu, G-c. Liu, T. Zhao, X. Liu), The Natural Science Foundation of the Jiangsu Higher Education Institutions of China (no. 23KJB320018 to Y. Pan), Leading Innovative Talents in Changzhou (no. 2021TQ0381, CQ20220129 to Y. Pan), Guangzhou Science and Technology Projects (no. 202201010910 to Z. Chen), Youth Medical Innovation and Practice Research Program of Guangzhou (no. 2023QNYXZD005 to J. Wei).

Note

Supplementary data for this article are available at Cancer Research Online (http://cancerres.aacrjournals.org/).

Received August 22, 2023; revised January 2, 2024; accepted February 16, 2024; published first February 21, 2024.

References

1. Siegel RL, Miller KD, Fuchs HE, Jemal A. Cancer statistics, 2021. CA Cancer J Clin 2021;71:7–33.
2. Cho YH, Kim MS, Chung HS, Hwang EC. Novel immunotherapy in metastatic renal cell carcinoma. Investig Clin Urol 2017;58:220–7.
3. Motzer RJ, Jonasch E, Agarwal N, Alva A, Baine M, Beckermann K, et al. Kidney Cancer, Version 3.2022, NCCN clinical practice guidelines in oncology. J Natl Compr Canc Netw 2022;20:71–90.
4. Williamson SR, Taneja K, Cheng L. Renal cell carcinoma staging: pitfalls, challenges, and updates. Histopathology 2019;74:18–30.
5. Fridman WH, Pagès F, Sautès-Fridman C, Galon J. The immune contexture in human tumours: impact on clinical outcome. Nat Rev Cancer 2012;12:298–306.
6. Liu XD, Hoang A, Zhou L, Kalra S, Yetil A, Sun M, et al. Resistance to antiangiogenic therapy is associated with an immunosuppressive tumor microenvironment in metastatic renal cell carcinoma. Cancer Immunol Res 2015;3:1017–29.
7. Chevrier S, Levine JH, Zanotelli VRT, Silina K, Schulz D, Bacac M, et al. An immune atlas of clear cell renal cell carcinoma. Cell 2017;169:736–49.
8. Qu Y, Feng J, Wu X, Bai L, Xu W, Zhu L, et al. A proteogenomic analysis of clear cell renal cell carcinoma in a Chinese population. Nat Commun 2022;13:2052.
9. Frumento G, Rotondo R, Tonetti M, Damonte G, Benatti U, Ferrara GB. Tryptophan-derived catabolites are responsible for inhibition of T and natural killer cell proliferation induced by indoleamine 2,3-dioxygenase. J Exp Med 2002;196:459–68.
10. Munn DH, Shafizadeh E, Attwood JT, Bondarev I, Pashine A, Mellor AL. Inhibition of T cell proliferation by macrophage tryptophan catabolism. J Exp Med 1999;189:1363–72.
11. Shi D, Wu X, Jian Y, Wang J, Huang C, Mo S, et al. USP14 promotes tryptophan metabolism and immune suppression by stabilizing IDO1 in colorectal cancer. Nat Commun 2022;13:5644.
12. Zhai L, Bell A, Ladomersky E, Lauing KL, Bollu L, Nguyen B, et al. Tumor cell IDO enhances immune suppression and decreases survival independent of tryptophan metabolism in glioblastoma. Clin Cancer Res 2021;27:6514–28.
13. Mellor AL, Keskin DB, Johnson T, Chandler P, Munn DH. Cells expressing indoleamine 2,3-dioxygenase inhibit T cell responses. J Immunol 2002;168:3771–6.
14. Holmgaard RB, Zamarin D, Li Y, Gasmi B, Munn DH, Allison JP, et al. Tumor-expressed IDO recruits and activates MDSCs in a Treg-dependent manner. Cell Rep 2015;13:412–24.
15. Rothhammer V, FJ Q. The aryl hydrocarbon receptor: an environmental sensor integrating immune responses in health and disease. Nat Rev Immunol 2019;19:184–97.
16. Cheong JE, Sun L. Targeting the IDO1/TDO2-KYN-AhR pathway for cancer immunotherapy - challenges and opportunities. Trends Pharmacol Sci 2018;39:307–25.
17. Prendergast GC. Cancer: why tumours eat tryptophan. Nature 2011;478:192–4.
18. Liu Y, Liang X, Dong W, Fang Y, Lv J, Zhang T, et al. Tumor-repopulating cells induce PD-1 expression in CD8(+) T cells by transferring kynurenine and AhR activation. Cancer Cell 2018;33:480–94.
19. de Araújo EF, Feriotti C, Galdino NAL, Preite NW, Calich VLG, FV L. The IDO-AhR axis controls Th17/Treg immunity in a pulmonary model of fungal infection. Front Immunol 2017;8:880.
20. Ozturk S, Uysal F. Poly(A)-binding proteins are required for translational regulation in vertebrate oocytes and early embryos. Reprod Fertil Dev 2017;29:1890–901.
21. Wu YQ, Ju CL, Wang BJ, RG W. PABPC1L depletion inhibits proliferation and migration via blockage of AKT pathway in human colorectal cancer cells. Oncol Lett 2019;17:3439–45.
22. Hua X, Ge S, Chen J, Zhang L, Tai S, Liang C. Effects of RNA binding proteins on the prognosis and malignant progression in prostate cancer. Front Genet 2020;11:591667.
23. Gui CP, Wei JH, Chen YH, Fu LM, Tang YM, Cao JZ, et al. A new thinking: extended application of genomic selection to screen multiomics data for development of novel hypoxia-immune biomarkers and target therapy of clear cell renal cell carcinoma. Brief Bioinform 2021;22:bbab173.

24. Yang JF, Xing X, Luo L, Zhou XW, Feng JX, Huang KB, et al. Mitochondria-ER contact mediated by MFN2-SERCA2 interaction supports CD8(+) T cell metabolic fitness and function in tumors. Sci Immunol 2023;8:eabq2424.
25. Budhu S, Loike JD, Pandolfi A, Han S, Catalano G, Constantinescu A, et al. CD8+ T cell concentration determines their efficiency in killing cognate antigen-expressing syngeneic mammalian cells *in vitro* and in mouse tissues. J Exp Med 2010;207:223–35.
26. Pan Y, Lu X, Shu G, Cen J, Lu J, Zhou M, et al. Extracellular vesicle-mediated transfer of LncRNA IGFL2-AS1 confers sunitinib resistance in renal cell carcinoma. Cancer Res 2023;83:103–16.
27. Zhao E, Maj T, Kryczek I, Li W, Wu K, Zhao L, et al. Cancer mediates effector T cell dysfunction by targeting microRNAs and EZH2 via glycolysis restriction. Nat Immunol 2016;17:95–103.
28. Huang D, Chen J, Yang L, Ouyang Q, Li J, Lao L, et al. NKILA lncRNA promotes tumor immune evasion by sensitizing T cells to activation-induced cell death. Nat Immunol 2018;19:1112–25.
29. Zhang Y, Narayanan SP, Mannan R, Raskind G, Wang X, Vats P, et al. Single-cell analyses of renal cell cancers reveal insights into tumor microenvironment, cell of origin, and therapy response. Proc Nat Acad Sci U S A 2021;118:e2103240118.
30. Braun DA, Street K, Burke KP, Cookmeyer DL, Denize T, Pedersen CB, et al. Progressive immune dysfunction with advancing disease stage in renal cell carcinoma. Cancer Cell 2021;39:632–48.
31. Guzeloglu-Kayisli O, Lalioti MD, Babayev E, Torrealday S, Karakaya C, Seli E. Human embryonic poly(A)-binding protein (EPAB) alternative splicing is differentially regulated in human oocytes and embryos. Mol Hum Reprod 2014;20:59–65.
32. Hugo W, Zaretsky JM, Sun L, Song C, Moreno BH, Hu-Lieskovan S, et al. Genomic and transcriptomic features of response to Anti-PD-1 therapy in metastatic melanoma. Cell 2016;165:35–44.
33. Shin DS, Zaretsky JM, Escuin-Ordinas H, Garcia-Diaz A, Hu-Lieskovan S, Kalbasi A, et al. Primary resistance to PD-1 blockade mediated by JAK1/2 mutations. Cancer Discov 2017;7:188–201.
34. Yamashita N, Long M, Fushimi A, Yamamoto M, Hata T, Hagiwara M, et al. MUC1-C integrates activation of the IFN-γ pathway with suppression of the tumor immune microenvironment in triple-negative breast cancer. J Immunother Cancer 2021;9:e002115.
35. Guzeloglu-Kayisli O, Pauli S, Demir H, Lalioti MD, Sakkas D, Seli E. Identification and characterization of human embryonic poly(A) binding protein (EPAB). Mol Hum Reprod 2008;14:581–8.
36. Smith RWP, Anderson RC, Larralde O, Smith JWS, Gorgoni B, Richardson WA, et al. Viral and cellular mRNA-specific activators harness PABP and eIF4G to promote translation initiation downstream of cap binding. Proc Nat Acad Sci U S A 2017;114:6310–5.
37. Wang X, He Q, Shen H, Xia A, Tian W, Yu W, et al. TOX promotes the exhaustion of antitumor CD8(+) T cells by preventing PD1 degradation in hepatocellular carcinoma. J Hepatol 2019;71:731–41.
38. Dieu-Nosjean MC, Antoine M, Danel C, Heudes D, Wislez M, Poulot V, et al. Long-term survival for patients with non-small-cell lung cancer with intratumoral lymphoid structures. J Clin Oncol 2008;26:4410–7.
39. Pagès F, Kirilovsky A, Mlecnik B, Asslaber M, Tosolini M, Bindea G, et al. *In situ* cytotoxic and memory T cells predict outcome in patients with early-stage colorectal cancer. J Clin Oncol 2009;27:5944–51.
40. Denkert C, Loibl S, Noske A, Roller M, Müller BM, Komor M, et al. Tumor-associated lymphocytes as an independent predictor of response to neoadjuvant chemotherapy in breast cancer. J Clin Oncol 2010;28:105–13.
41. Galon J, Costes A, Sanchez-Cabo F, Kirilovsky A, Mlecnik B, Lagorce-Pagès C, et al. Type, density, and location of immune cells within human colorectal tumors predict clinical outcome. Science 2006;313:1960–4.
42. Zhang L, Conejo-Garcia JR, Katsaros D, Gimotty PA, Massobrio M, Regnani G, et al. Intratumoral T cells, recurrence, and survival in epithelial ovarian cancer. N Engl J Med 2003;348:203–13.
43. Remark R, Alifano M, Cremer I, Lupo A, Dieu-Nosjean MC, Riquet M, et al. Characteristics and clinical impacts of the immune environments in colorectal and renal cell carcinoma lung metastases: influence of tumor origin. Clin Cancer Res 2013;19:4079–91.
44. Jiang P, Gu S, Pan D, Fu J, Sahu A, Hu X, et al. Signatures of T cell dysfunction and exclusion predict cancer immunotherapy response. Nat Med 2018;24:1550–8.
45. Alissafi T, Hatzioannou A, Legaki AI, Varveri A, Verginis P. Balancing cancer immunotherapy and immune-related adverse events: the emerging role of regulatory T cells. J Autoimmun 2019;104:102310.
46. Kolb HR, Borcherding N, Zhang W. Understanding and targeting human cancer regulatory T cells to improve therapy. Adv Exp Med Biol 2021;1278:229–56.
47. Liu M, Wang X, Wang L, Ma X, Gong Z, Zhang S, et al. Targeting the IDO1 pathway in cancer: from bench to bedside. J Hematol Oncol 2018;11:100.
48. Muller AJ, Sharma MD, Chandler PR, Duhadaway JB, Everhart ME, Johnson BA 3rd, et al. Chronic inflammation that facilitates tumor progression creates local immune suppression by inducing indoleamine 2,3 dioxygenase. Proc Nat Acad Sci U S A 2008;105:17073–8.
49. Prendergast GC, Mondal A, Dey S, Laury-Kleintop LD, Muller AJ. Inflammatory reprogramming with IDO1 inhibitors: turning immunologically unresponsive 'Cold' tumors 'Hot'. Trends Cancer 2018;4:38–58.
50. Smith C, Chang MY, Parker KH, Beury DW, DuHadaway JB, Flick HE, et al. IDO is a nodal pathogenic driver of lung cancer and metastasis development. Cancer Discov 2012;2:722–35.
51. Moyer BJ, Rojas IY, Murray IA, Lee S, Hazlett HF, Perdew GH, et al. Indoleamine 2,3-dioxygenase 1 (IDO1) inhibitors activate the aryl hydrocarbon receptor. Toxicol Appl Pharmacol 2017;323:74–80.
52. Metz R, Rust S, Duhadaway JB, Mautino MR, Munn DH, Vahanian NN, et al. IDO inhibits a tryptophan sufficiency signal that stimulates mTOR: a novel IDO effector pathway targeted by D-1-methyl-tryptophan. Oncoimmunology 2012;1:1460–8.
53. Gordziel C, Bratsch J, Moriggl R, Knösel T, Friedrich K. Both STAT1 and STAT3 are favourable prognostic determinants in colorectal carcinoma. Br J Cancer 2013;109:138–46.
54. Osborn JL, Greer SF. Metastatic melanoma cells evade immune detection by silencing STAT1. Int J Mol Sci 2015;16:4343–61.